Numerical simulation of the flow field around a propeller

Bogdan Darie

Master Thesis

presented in partial fulfillment
of the requirements for the double degree:
“Advanced Master in Naval Architecture” conferred by University of Liege
"Master of Sciences in Applied Mechanics, specialization in Hydrodynamics, Energetics and Propulsion” conferred by Ecole Centrale de Nantes

developed at "Dunărea de Jos" University, Galaţi
in the framework of the

“EMSHIP”
Erasmus Mundus Master Course
in “Integrated Advanced Ship Design”

Ref. 159652-1-2009-1-BE-ERA MUNDUS-EMMC

Supervisor:	Prof. Mihaela Amorăriţei, "Dunărea de Jos" University of Galaţi
Reviewer:	Prof. André Hage, University of Liege

Galaţi, February 2012

This page is intentionally left blank.

ABSTRACT

Numerical simulation of the flow field around a propeller

By **Bogdan Darie**

This paper reflects the scientific research which I conducted during my Erasmus Mundus master course, especially in the third semester spent at "Dunărea de Jos" University of Galaţi.

Computational Fluid Dynamics (CFD) methods have become a very important tool in ship design: resistance, propulsion, maneuverability, etc. Regarding ship propulsion, CFD codes represent a new capability to greatly improve the design and analysis process of the propellers, in conjunction with experimental tests and analytical methods based on circulation theory and standard series.

Accurate and reliable propeller performances predictions are a fundamental aspect for any analysis and design of a modern propeller. Cavitation and cavity extension are other important problems that influence the efficiency of a propeller, in addition to propagated noise, blade vibration and erosion. Nevertheless, this field of research will not be treated in the presented work.

The Potsdam Propeller Test Case (PPTC) within the SMP Workshop on Cavitation and Propeller Performances represents an excellent chance to test and to validate the abilities achieved in predicting the performances of propellers in open water.

In this paper, the open water performances of the SMP11's propeller (cf. figure below) will be numerically simulated using a commercial CFD code based on RANS solver with a hybrid mesh. In the following the propeller geometry is known, the methods used are described, as well as the results and conclusions of the analysis and of the experimental tests, from the SMP'11 Workshop on Propeller Performance: Potsdam Propeller Test Case.

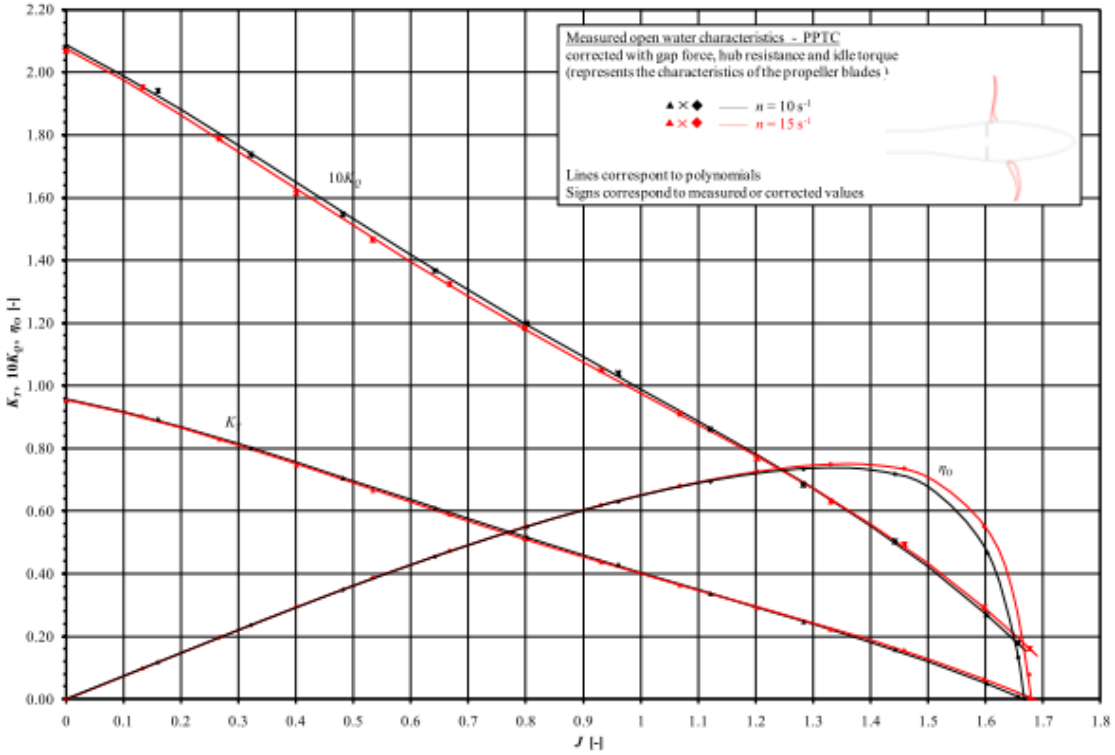

PPTC test results

ABSTRAIT

Simulation numérique du champ de flux autour d'une hélice

Par **Bogdan Darie**

Ce papier reflète la recherche scientifique que j'ai menée pendant mon cursus de master Erasmus Mundus, surtout pendant le troisième semestre passé à l'université de Galaţi « Dunărea de Jos ».

Les méthodes de CFD (« Computational Fluid Dynamics ») sont devenues un instrument important pour la conception navale : résistance, propulsion, manœuvrabilité, etc. Concernant la propulsion navale les codes de CFD représentent une nouvelle capacité pour beaucoup améliorer la conception et le processus d'analyse des hélices, conjointement avec des tests expérimentaux et des méthodes analytiques basés sur la théorie de circulation et les séries standard.

Les prédictions exactes et fiables de la performance des hélices font partie fondamentale de toute analyse et toute conception d'une hélice moderne. La cavitation et l'extension de la cavité sont des autres problèmes importants qui influencent l'efficacité, en plus du bruit propagé, de la vibration des pales et de l'érosion. Néanmoins, ce domaine de recherche ne sera pas traité dans le travail présenté.

Le « Potsdam Propeller Test Case » (PPTC) au sein du « SMP Workshop on Cavitation and Propeller Performances » représente une occasion excellente pour tester et valider les compétences obtenues dans la prédiction des performances d'hélices en eau libre.

Dans ce papier, les performances en eau libre de l'hélice SMP11 (cf. figure en bas) seront simulées numériquement, utilisant un code de CFD commercial basé sur « RANS solver » avec un maillage déstructuré. Dans le suivant, la géométrie de l'hélice est connue, les méthodes utilisées sont décrites, aussi les résultats et les conclusions de l'analyse et des tests expérimentaux du « SMP11 Workshop on Propeller Performance: Potsdam Propeller Test Case ».

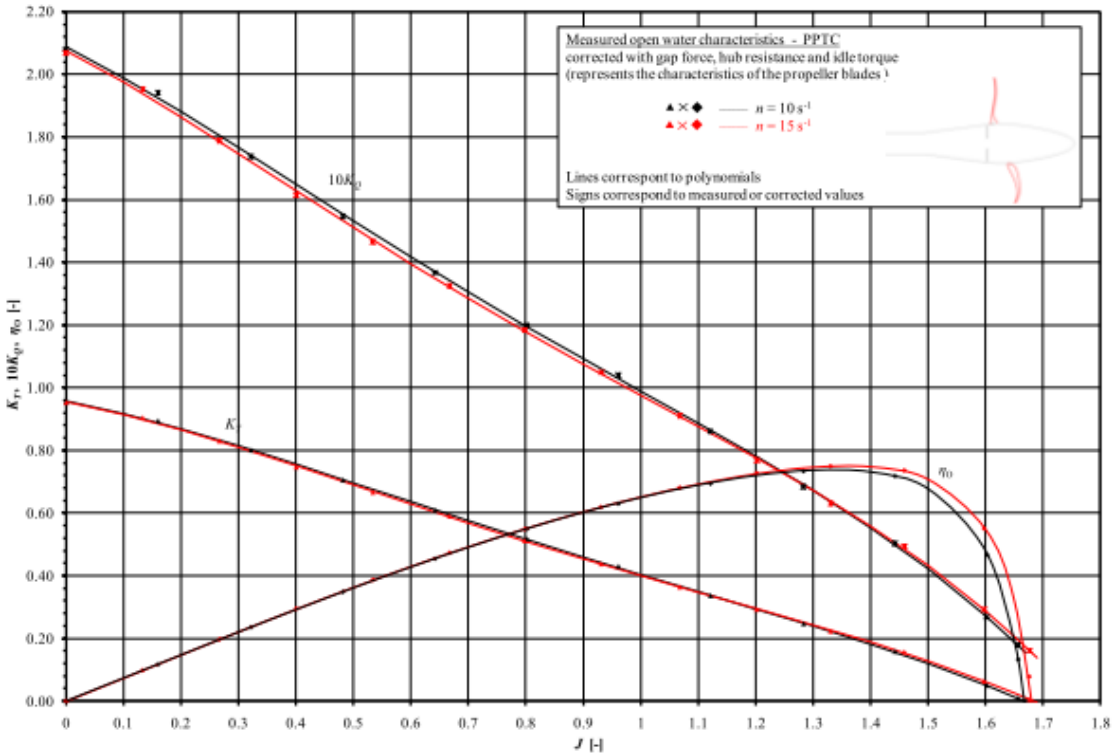

Résultats du test PPTC

ACKNOWLEDGEMENTS

This thesis was developed in the frame of the European Master Course in "Integrated Advanced Ship Design" named "EMSHIP" for "European Education in Advanced Ship Design", Ref.: 159652-1-2009-1-BE-ERA MUNDUS-EMMC.

First of all, I would like to express my sincere appreciation and gratitude to my Mum and Dad for their unconditioned love and support, not only during this Master Course, but throughout my whole life. I am so lucky to be their son and to them I dedicate this thesis.

Special thanks to Andra Gherman whom encouraged me to join this program and for her constant support, I wouldn't be here if it wouldn't be for her.

Many thanks to prof. Leonard Domnişoru for every priceless advice he gave, and for tutoring me in the professional life.

Additionally, I would like to thank all those that assisted me in developing this thesis.

I would like to express my gratefulness to my colleagues of the EMSHIP Course, the teachers and all the administrative stuff for making this possible.

Galaţi, February 2012

Bogdan Darie

This page is intentionally left blank.

CONTENTS

This page is intentionally left blank.

Declaration of Authorship

I declare that this thesis and the work presented in it are my own and have been generated by me as the result of my own original research.

Where I have consulted the published work of others, this is always clearly attributed.

Where I have quoted from the work of others, the source is always given. With the exception of such quotations, this thesis is entirely my own work.

I have acknowledged all main sources of help.

Where the thesis is based on work done by myself jointly with others, I have made clear exactly what was done by others and what I have contributed myself.

This thesis contains no material that has been submitted previously, in whole or in part, for the award of any other academic degree or diploma.

I cede copyright of the thesis in favour of "Dunărea de Jos" University of Galaţi.

Date: *Signature*

24.01.2010

This page is intentionally left blank.

List of figures

List of tables

1. OVERVIEW

Propellers create thrust as each of the blades is subject to local lift forces. Ideally, this lift is created with minimum drag losses, which is the basically the same goal for any other foil flows, e.g. airfoils, ship rudders etc. Each propeller section resembles a cross-section of a foil. However, unlike aeronautical foils, ship propellers feature short and stubby blades with a much smaller span ratio than in aeronautical foils. The reduced dimensions of the propellers are given by the position of it and the high probability of cavitation phenomena to arise.

The design of a propeller is based on three stages: preliminary design, detailed design and analysis. First step is based on systematic series and can offer information about propeller diameter, number of blades, pitch ratio or expanded area ratio, which give a good agreement between shaft power, propeller revolution and ship speed. These results are used as input data for the second stage, where the lifting line theory with lifting surface corrections is used. At this stage the geometry of the propeller is obtained, with some approximations of the working environment, and the process can continue with the analysis of the obtained geometry. This analysis consists in finding the pressure distribution, evaluation of the hydrodynamic performances in off-design conditions and investigation of the influence of ship's wake on the cavitation performances and vibration induced by the propeller. Nevertheless if the geometry is already known, one can use the second stage of the design to investigate the performances that can be achieved with it.

One of the main interest in propeller design is to obtain the propeller characteristics (open water characteristics); to be sure that the design fulfills the requirements, after which a verification of cavitation phenomena is performed.

A lot of researchers try to improve the methods by which these tasks can be performed with high accuracy but with low cost (computation, man-hour).

Among the methods that can be used for propeller design it can be noticed: momentum theory, Lifting-line method, Lifting-surface method (especially vortex-lattice method), Boundary element method/panel method, RANS method – each of them with their pros and cons.

Due to the small span-to-chord ratio of a ship propeller blade, the flows around it are rather complex. All two-dimensional approaches to model the flow around a propeller blade (like lifting-line theories) introduce considerable errors that must be corrected afterwards. Lifting-line approaches are still popular in propeller design as a preliminary step, before more powerful, but also more expensive, three-dimensional methods are employed.

Nowadays a high interest in propeller performance is being taken, due to the fact that this is tightly connected to ship resistance and therefore to the fuel consumption.

The introduction of high-skew propellers necessitates truly three-dimensional theories to model the flow around the propeller. Empirical corrections for the lifting-line method could no longer be applied satisfactorily to the new and more complex propeller geometries. The approach is then to use lifting-line methods for an initial design serving as a starting point for more sophisticated methods.

A skewed controllable pitch propeller with extensive measurement data was provided by SVA Potsdam with well-defined cases and conditions for the SMP'11 Workshop on Cavitation and Propeller Performance [4]. The experiment datasets cover the open water characteristics, LDV measurements of velocity field (non-cavitating) and cavitation tests.

According to workshop specifications, the computational model will be applied to the analysis of a five-bladed controllable pitch right-handed propeller. Main geometry parameters are described in Chapter 3. In the first step a simpler approach of performances investigation is performed using the lifting line theory. After which a more sophisticated method is applied using CFD methods. Steady incompressible RANS method, with a realizable k-ε turbulence model available in commercial solver FLUENT, is used in the beginning. The turbulence model is changed in the second part to a one equation model, Spalart-Allmaras. Calculations results of the open water characteristics are presented in Chapter 9. A comparison between experimental results and numerical simulation is made in the end of this paper.

2. INTRODUCTION

One of the first who made use of the of computational fluid dynamics [3] was Kopal, which in 1947 compiled massive tables of the supersonic flow over sharp cones by numerically solving the governing differential equations (the Taylor–Maccoll equation). These solutions were carried out on a primitive digital computer at the Massachusetts Institute of Technology.

The beginning of CFD was triggered by the availability of powerful workstations and even now the progresses in CFD are still tightly coupled with the evolution of computer technology.

In the beginning of the 1980's, the solution of first two-dimensional (2-D) and later also three-dimensional (3-D) Euler equations became possible. With the mid 1980's, the focus started to shift to the significantly more demanding simulation of viscous flows governed by the Navier-Stokes equations. Together with this, a variety of turbulence models evolved with different degree of numerical complexity and accuracy. The leading edge in turbulence modeling is represented by the Direct Numerical Simulation (DNS) and the Large Eddy Simulation (LES). However, both approaches are still far away from being usable in engineering applications.

Computational fluid dynamics provides the convenience of being able to switch off specific terms in the governing equations. This permits the testing of theoretical models and, inverting the connection, suggesting new paths for theoretical exploration.

The quality of simulation results depends on the choice of the model and on the accuracy of the numerical method. In spite of the inevitable numerical and modeling errors, approximate solutions may provide a lot of valuable information at a fraction of the cost that a full-scale experimental investigation would require.

A further advantage of the computational approach is the fact that it can be applied to flows in domains with arbitrarily large or small dimensions under realistic operating conditions. Last but not least, simultaneous computation of instantaneous density, velocity, pressure, temperature, and concentration fields is possible. It is known that no experimental method can capture the values and the evolution of all flow variables throughout the domain.

The design tools for propellers have evolved in two different directions, one being the testing and the other the analytical/calculating. Through the last century they have supported each other well and both have contributed to the understanding of the propeller and the conditions in which it works.

Some differences between experimental and numerical simulations are summarized in Table 1. However experiments are still required to determine the values of input parameters for a mathematical model and to validate the computational results.

Numerical simulation cannot solve everything (and experiments not either), CFD and experiments are complementary ways to understand, analyze and solve different problems.

Table 1 Experiment-Simulation differences

Experiments	Simulations
Quantitative description of flow phenomena	Quantitative prediction of flow phenomena
For one quantity at a time	For all desired quantities
At a limited number of points and time instants	With high resolution in space and time
For a laboratory-scale model	For the actual flow domain
For a limited range of problems and operating conditions	For any virtual problem and realistic operating conditions
Error sources: measurement errors, flow disturbances by the probes	Error sources: modeling, discretization

Marine propellers with various blade geometry, such as a highly skewed propeller, are often fitted to ships in order to improve the cavitation performance, to reduce the propeller-induced vibration and noise, or to improve the efficiency of the propeller. In the design of such propellers, the design charts based on methodical series tests are to be supplemented by the theoretical calculations of propeller open-water characteristics.

3. PROPELLER MODEL

As it was mentioned in this paper will be studied the open water performances of the SMP11's propeller (Figure 1) with the characteristics presented in Table 2.

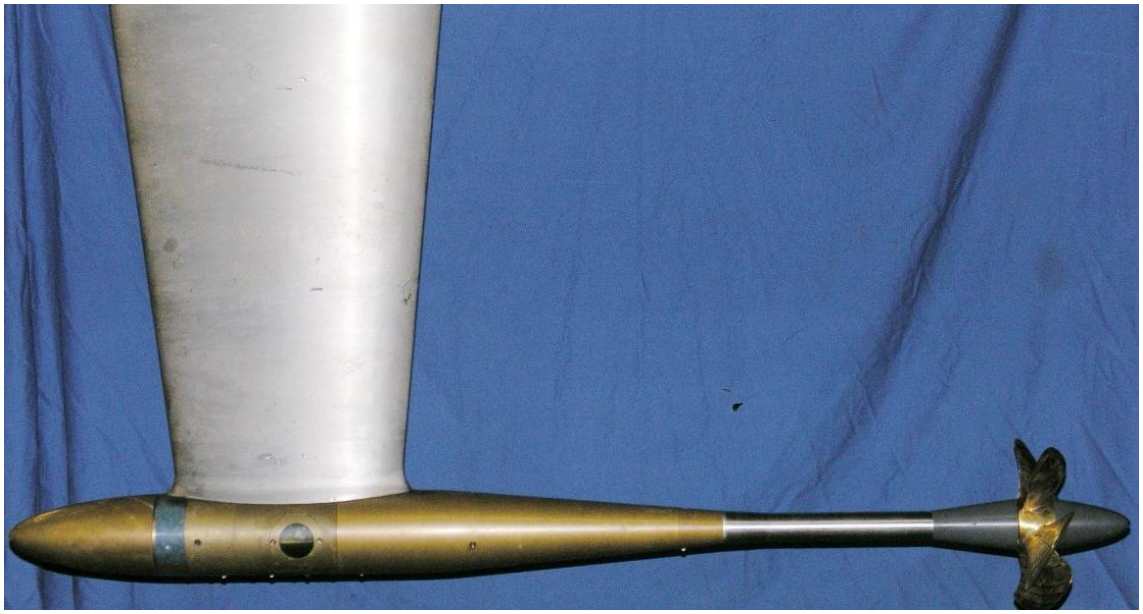

Figure 1 SMP'11 propeller

Table 2 Propeller characteristics

Propeller diameter	D	[mm]	250.000
Pitch at r/R=0.7	$P_{0.7}$	[mm]	408.750
Pitch at r/R=0.75	$P_{0.75}$	[mm]	407.380
Mean pitch	P_{mean}	[mm]	391.881
Chord length at r/R =0.7	$C_{0.7}$	[mm]	104.167
Chord length at r/R=0.75	$C_{0.75}$	[mm]	106.347
Thickness at r/R=0.75	$T_{0.75}$	[mm]	3.791
Pitch ratio	$P_{0.7}/D$	[-]	1.635
Mean pitch ratio	P_{mean}/D	[-]	1.567
Area ratio	A_E/A_o	[-]	0.779
Skew	Θ_{eff}	[^{0}]	18.800
Hub diameter ratio	d_h/D	[-]	0.150
Number of blades	z	[-]	5
Direction of rotation			Right-handed(SCS)*

*the direction of rotation is given in the ship coordinate system Figure 3

Along with the data of the propeller presented in APPENDIX A, the workshop provided also the geometry (Figure 2) of the propeller presented in Figure 1.

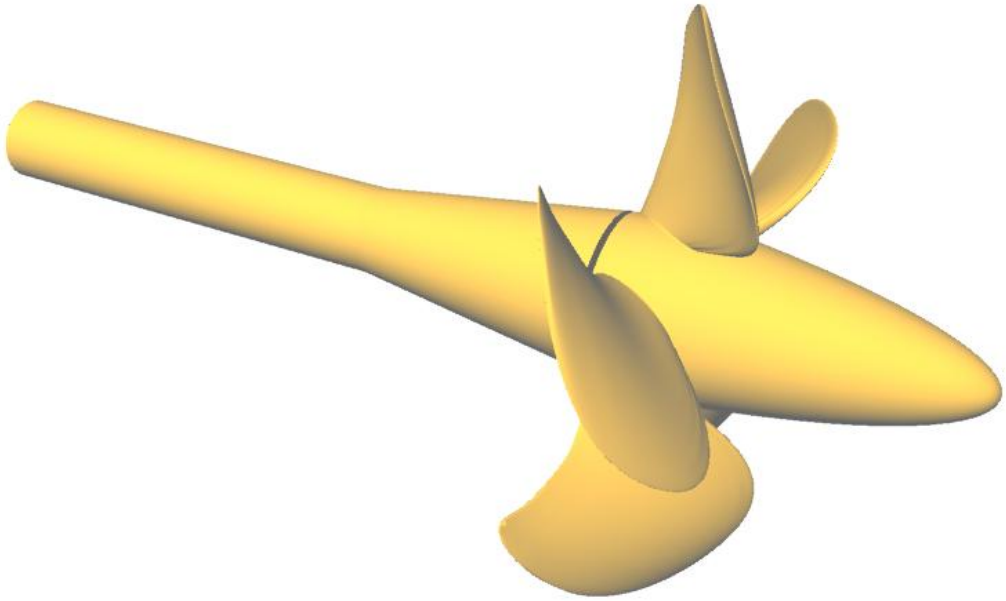

Figure 2 Propeller geometry

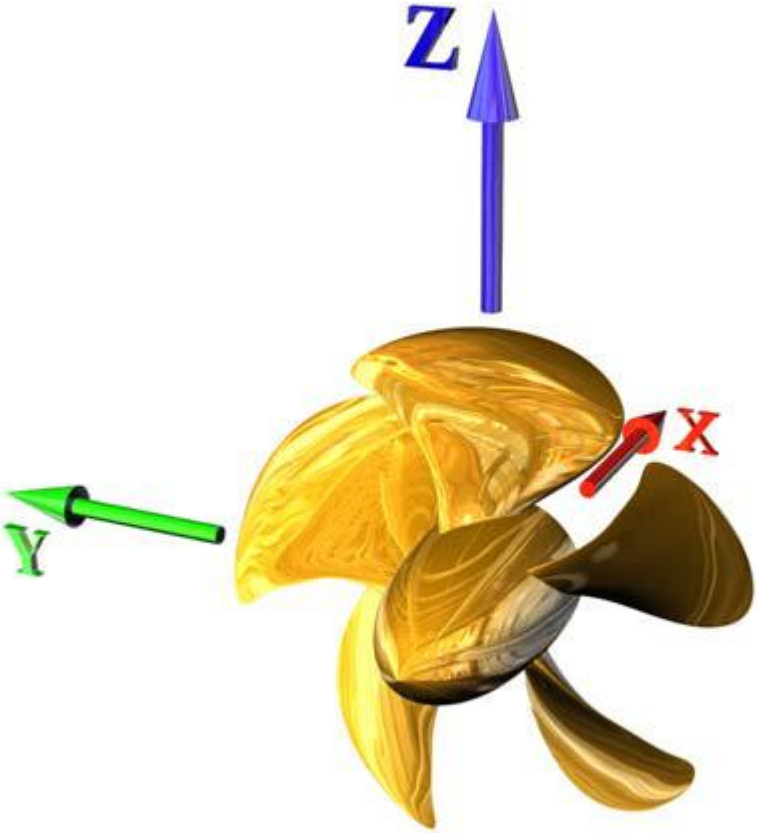

Figure 3 Ship coordinate

4. OPEN WATER CHARACTERISTICS

Before the numerical simulation, the open water characteristics of a propeller are introduced.

The propeller performances are characterized by the trust, torque and efficiency. These are usually expressed as functions of rpm *n* in non-dimensional form as:

$$K_T = \frac{T}{\rho * n^2 * D^4}$$
$$K_Q = \frac{Q}{\rho * n^2 * D^5} \quad (1)$$

The force T is made non-dimensional by the propeller disk area times the stagnation pressure based on the circumferential speed, omitting a factor $\pi^2/8$.The moment Q is made non-dimensional by the additional length, i.e. the propeller diameter D.

The advance number J is defined as:

$$J = \frac{V_A}{nD} \quad (2)$$

,where V_A is the average inflow speed to the propeller.

The propeller open-water efficiency is derived from thrust and torque coefficients and the advance number:

$$\eta_0 = \frac{P_T}{P_D^{'}} = \frac{T * V_A}{2\pi * n * Q} = \frac{K_T * \rho * n^2 * D^4}{K_Q * \rho * n^2 * D^5} * \frac{V_A}{2\pi * n} = \frac{K_T}{K_Q} * \frac{J}{2\pi} \quad (3)$$

,where the ratio between the propeller's efficiency attached to a ship P_D and in open water $P_D^{'}$ is termed relative rotative efficiency.

The trust and torque coefficients and efficiency of the propeller are displayed in diagrams as curves over *J*. These curves are mainly used for propeller optimization and to determine the operation point (rpm, thrust, torque, power) of the ship. While the use of diagrams in education is still popular, in practice computer programs are almost exclusively used in propeller design. For propeller series, with extensive experimental data, the curves are represented traditionally as polynomials in the form:

$$K_T = \sum C_T * J^S * \left(\frac{P}{D}\right)^t * \left(\frac{A_E}{A_0}\right)^u * Z^v \quad (4)$$

While this may appear tedious, it is easy to program and fast to evaluate either by higher programming languages or spreadsheets. Diagrams (Figure 4) are still popular in practice for documentation and visualization of tendencies. In keeping with common practice, KQ is multiplied by ten in order to better present the curves on one set of axes.

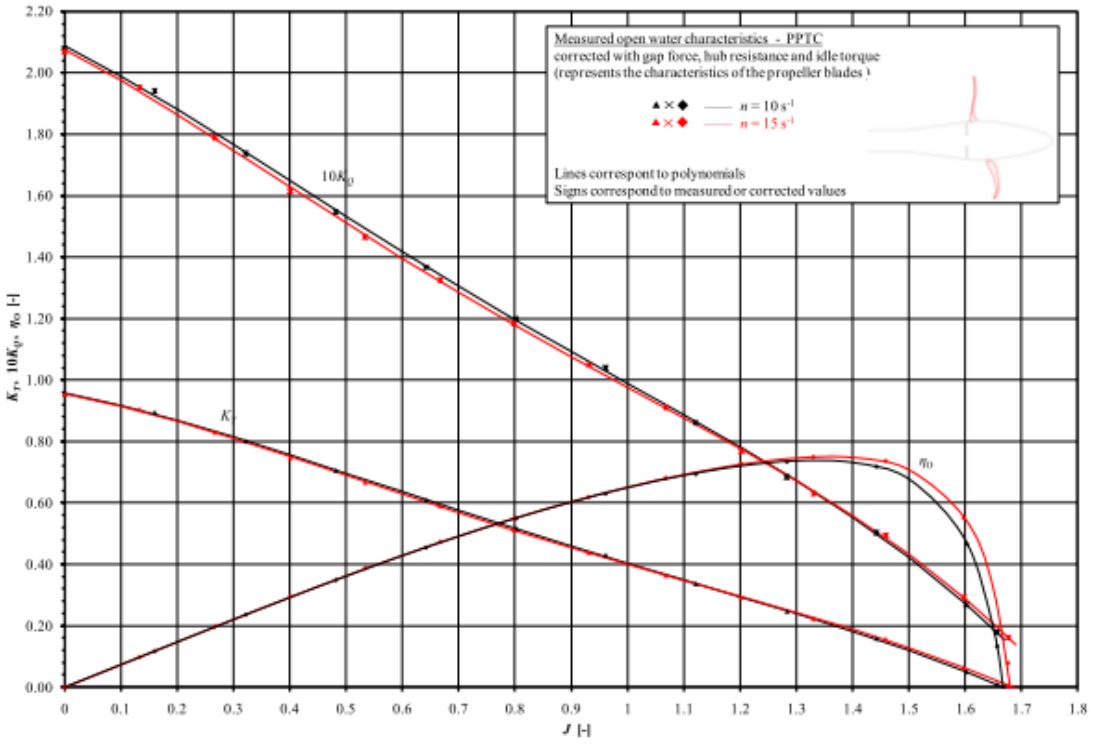

Figure 4 Open water characteristics diagram

Another important open-water parameter is the thrust loading coefficient:

$$C_{Th} = \frac{T}{\rho * V_A^2 * D^2 * \pi/8} \tag{5}$$

This coefficient makes the thrust non-dimensional with the propeller disk area times stagnation pressure based on the propeller inflow velocity. Sometimes C_{Th} is also plotted explicitly in propeller characteristics diagrams, but sometimes it is omitted as it can be derived from the other quantities.

Depending on the combination of ship's heading and the propeller thrust, it can be distinguished four cases:

- ship has forward speed, propeller delivers forward thrust
- ship has forward speed, propeller delivers reverse thrust
- ship has reverse speed, propeller delivers forward thrust
- ship has reverse speed, propeller delivers reverse thrust

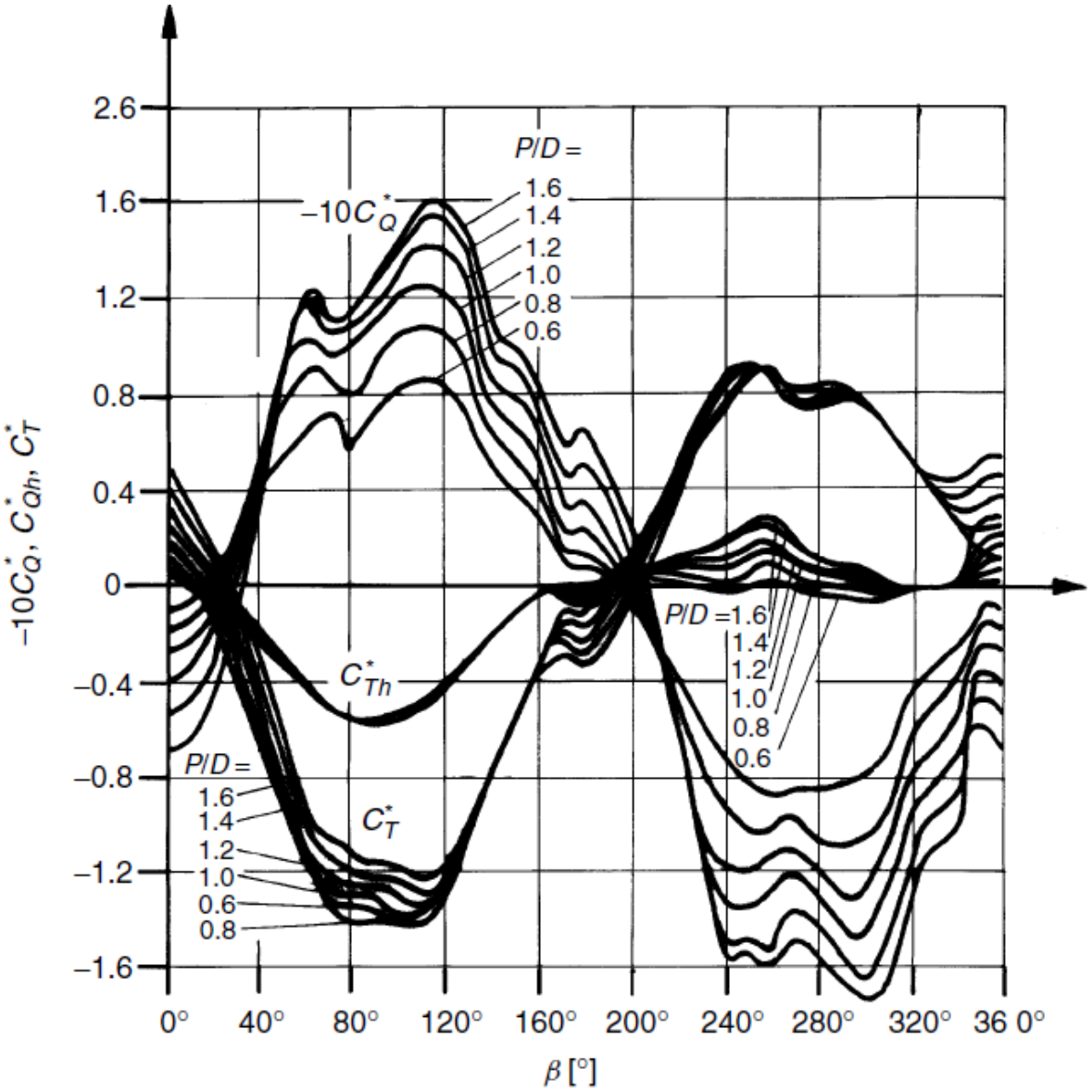

Figure 5 Four-quadrant diagram for propellers [6]

These diagrams contain the open water characteristics for special cases and are available only for some selected propellers. They are considerable harder to obtain and they are mainly used in computer simulations of ship maneuvers. They have on the abscissa the effective advance angle β defined by (6) and they represent the non-dimensional modified thrust and torque coefficients, (7) and respectively (7).

$$\tan\beta = \frac{V_A}{0.7\pi * n * D} \tag{6}$$

$$C_{Th}^{*} = \frac{T}{\rho * V_R^2 * \pi * D^2 / 8} \tag{7}$$

$$C_Q^{*} = \frac{Q}{\rho * V_R^2 * \pi * D^3 / 8} \tag{8}$$

5. A SIMPLE APROACH

In the first step, of producing the open water diagram, it will be used the lifting line theory. In this theory the blade is replaced by a straight line, the circulation, Γ, about the blade associated with lift is replaced by a vortex filament. The vortex filament lies along the straight line; and, at each span-wise station, the strength of the vortex is proportional to the local intensity of lift. According to Helmholtz's theorem, a vortex filament cannot terminate in the fluid. The variation in vortex strength is therefore assumed to result from superposition of a number of horseshoe shaped vortices, as shown in Figure 6. The portions of the vortices lying along the span are called the bound vortices. The portions of the vortices extending downstream indefinitely are called the trailing or free vortices.

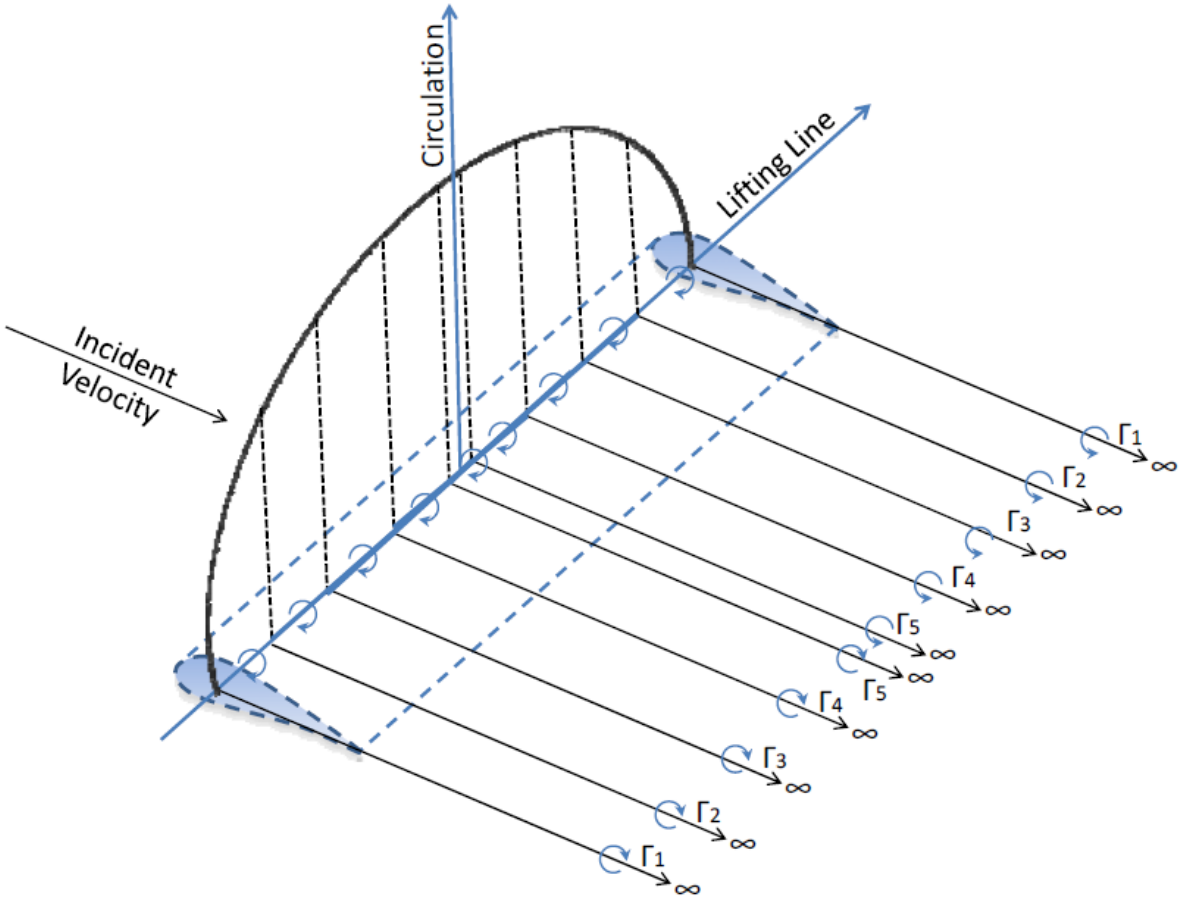

Figure 6 Vortex Pattern Representing a Lifting Wing

The effect of the trailing vortices, corresponding to a positive lift, is to induce a downward component of velocity at and behind the blade. This downward component is

called the downwash. The magnitude of the downwash at any section along the span is equal to the sum of the effects of all of the trailing vortices along the entire span. The effect of the downwash is to change the relative direction of the fluid stream over the section. The section is assumed to have the same hydrodynamic characteristics with respect to the rotated stream as it had in the normal two-dimensional flow.

According to the lifting-line theory, the propeller is replaced by a vortex system and the induced velocities in the propeller plane can be calculated without knowing the propeller geometry. The downwash affects not only the blade being modeled, but also every other blade on the propeller. However, if the propeller is symmetrical, these affects will cancel each other out. Therefore, the free vortices that are shed from the lifting line will be identical and spaced at constant angles to each other. The free vortex lines shed from the lifting line are not acted on by forces. Their directions, according to wing theory, coincide with that of the resultant lifting system. This results in the free vortex lines of a propeller, forming a general helical shape. When all of the free vortex lines are combined, they form a free vortex sheet that is in the shape of a general helical surface.

For practical application in the field of marine propeller, Lerbs and Goldstein [2] have been introduced "induction factors" – function with which the circulation and induced velocities are calculated, for given values of *J*, using the hydrodynamic properties of the foil sections at specified radial distances along the propeller blade.

There are two possible ways to determine the velocity field of symmetrically spaced helical vortex lines, the integral by Biot-Savart and Laplace's differential equation [2]. The Laplace equation approach provides numerical results more readily than the elaborate numerical integration following the Biot-Savart method [7].

If it is considered a propeller of *g* blades modeled as a symmetric system of *g* helical tip vortices combined with an axial hub vortex, which has the same strength as the entire tip vortices combined, the potential functions are only justified when assuming that the vortex system is infinitely long in both directions of the axis. By subtracting the potential of the hub vortex from this expression, we obtain the potential for an infinitely long symmetrical system of *g* helical vortices of constant radius, r_0, and constant pitch angle, β_{io}. First, a cylindrical coordinate system (z, ψ, r) is defined where *z* equals zero at the propeller and is positive in the direction of flow, and ψ equals zero at the first lifting line. Then the potential for internal points ($r< r_o$) in the field is defined by equation (9), and the potential for external points ($r>r_o$) is defined by equation (10). [1]

$$\Phi_i = \frac{g}{2}\overline{\Gamma} + \frac{g}{2\pi}\overline{\Gamma}\{\frac{z}{k_0} + 2\frac{r_0}{k_0}\sum_{n=1} I_{ng}\left(\frac{ng}{k_0}r\right)K'_{ng}\left(\frac{ng}{k_0}r_0\right)\sin ng\nu\} \quad (9)$$

$$\Phi_i = \frac{\overline{\Gamma}}{2\pi}\{g\Psi - 2\pi\sum_{m=1}^{g}\frac{m-1}{g} + 2g\frac{r_0}{k_0}\sum_{n=1} K_{ng}\left(\frac{ng}{k_0}r\right)I'_{ng}\left(\frac{ng}{k_0}r_0\right)\sin ng\nu\} \quad (10)$$

In order to find the induced velocities at a lifting line of the propeller, the above equations can be used with ψ and *z* both equal to zero. However, these velocities would correspond to a vortex system that extends from *z* equals positive infinity to negative infinity which is essentially a two-dimensional system. The vortex system of an actual propeller is three-dimensional and the vortex system extends only from *z* equals zero to positive infinity. In order to determine if velocities of the three-dimensional system could be determined from the two-dimensional system, Lerbs considered the velocity-integrals by Biot-Savart for the assumed case that both r_o and β_{io} are independent of ψ. It was concluded from these integrals that the effect of the axial and tangential components of the system between *z* equals negative infinity and the propeller (z=0) is equal to the effect of the system between the propeller and *z* equals positive infinity for points on the lifting line [8]. Therefore it follows that the axial, w_a, and tangential, w_t, velocities induced at a lifting line of a propeller are simply half the axial and tangential velocities induced from the potentials in equations (9) and (10).

Unfortunately, numerical accuracy of the induced velocities is degraded when the reference radius approaches the vortex radius because the expressions go to infinity. This problem can be avoided by using the induction factors from as defined in equations (11) and (12). The induction factors are the induced velocity non-dimensional components by the velocity induced at *r* by a straight potential vortex extending from *z* equals zero to positive infinity of strength Γ situated at r_o. Both the induced velocities and the non-dimensional velocity become infinite in the same order as *r* approaches r_o. Therefore, the induction factors remain finite as the radii approach each other. Combining the induced velocity equations into the induction factor equations yields the final induction factors as shown in equations (13) through (16).

$$i_a = \frac{\frac{\overline{w}_a}{\Gamma}}{4\pi(r - r_0)} \tag{11}$$

$$i_t = \frac{\frac{\overline{w}_t}{\Gamma}}{4\pi(r - r_0)} \tag{12}$$

$$i_{ai} = g\frac{x}{x_0 \tan(\beta_{io})}\left(\frac{x_0}{x} - 1\right)(1 + B_2) \tag{13}$$

$$i_{ae} = -g\frac{x}{x_0 \tan(\beta_{io})}\left(\frac{x_0}{x} - 1\right)B_1 \tag{14}$$

$$i_{ti} = g\left(\frac{x_0}{x} - 1\right)B_2 \tag{15}$$

$$i_{te} = -g\left(\frac{x_0}{x} - 1\right)(1 + B_1) \tag{16}$$

It is interesting to note that the induction factors are functions of geometric properties (i.e. the relative position of the reference point and where the vortex is shed as well as the angle at which it is shed) and are not dependents on the circulation. Also to be noted that the above expressions apply to only one lifting line. In general, there will also be induced velocities at each lifting line (i.e. each blade) from all other lifting lines. However, if the propeller is symmetric, these effects will cancel each other out.

When multiple vortex lines are shed from the same lifting line, a vortex sheet is formed. The velocity components which are produced by the vortex sheets are obtained by integrating the effects of the vortex lines over the span of the lifting line. By integrating over the free vortices and using equations (11) and (12), expressions for the induced velocities (non-dimensionalized with the speed of advance) at station x of the lifting line are shown in equations (17) and (18).

$$\frac{w_a}{V_S} = \frac{1}{2}\int_{x_h}^{1} \frac{dG}{dx_0}\frac{1}{x - x_0} i_a dx_0 \tag{17}$$

$$\frac{w_t}{V_S} = \frac{1}{2}\int_{x_h}^{1} \frac{dG}{dx_0}\frac{1}{x - x_0} i_t dx_0 \tag{18}$$

The vortex sheets described above are made up of cylindrical vortex lines whose pitch does not change in the axial direction. The next step is to determine the conditions imposed on the variations of the pitch of the vortex lines in the radial direction such that the entire system accurately models the vortex system of an actual propeller.

The force and the flow generated at a lifting line by the vortex sheets can be related using an energy balance of the propeller flow. The input power equals the useful power plus the increase in kinetic energy within the volume that passes through the slipstream in a single unit of time. Input power is also made up of an external input plus the work done by the centrifugal pressure on the volume of water in a single unit of time. The energy balance takes the form of equation (19) where the integral is taken over a disc with the same diameter as the propeller and ΔE is the kinetic energy of the induced flow within the volume of fluid that passes a point in the ultimate wake in one unit of time 68[1].

$$\int_{A}(r\omega dQ - vdT) = \Delta E \tag{19}$$

Knowing the geometry and polar curves of a propeller, it is possible to estimate the circulation and induced velocity distributions for a given advance ratio. To derive the relationship between the lift coefficient and the circulation at any radius along the blade we can use equation (20) according Figure 7. The solidity of the propeller, s, is defined in equation (21) where *l* is the chord length at a specified radius.

$$C_L s = \frac{2gGv}{V} \tag{20}$$

$$s = \frac{gl}{\pi D} \tag{21}$$

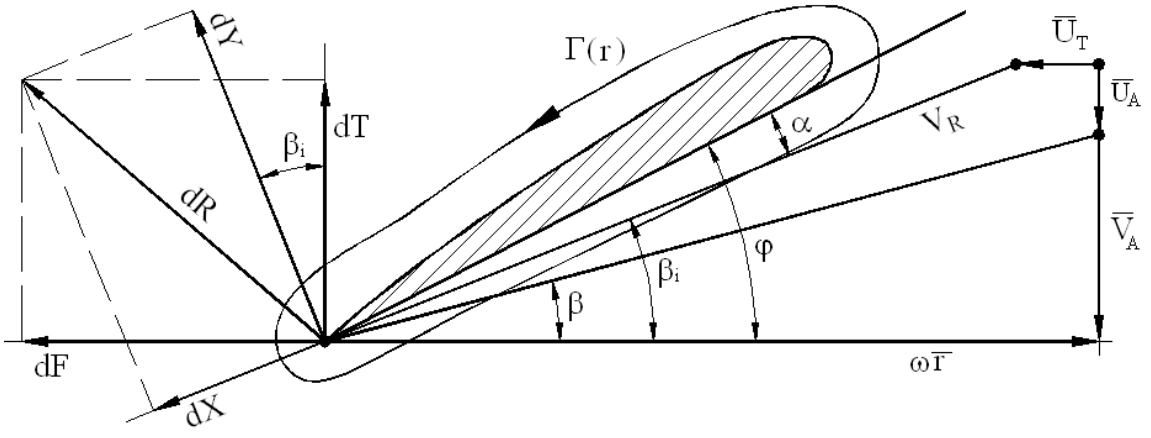

Figure 7 Velocity diagram [2]

In the end it can be computed the circulation distribution and the induced velocities for *m* stations along the propeller blade. In order to obtain these parameters more easily for many stations the above theory has been introduced in diverse computer codes [20]. One of them is the open source OpenProp v2.4.6 (Figure 8) developed by Massachusetts Institute of Technology.

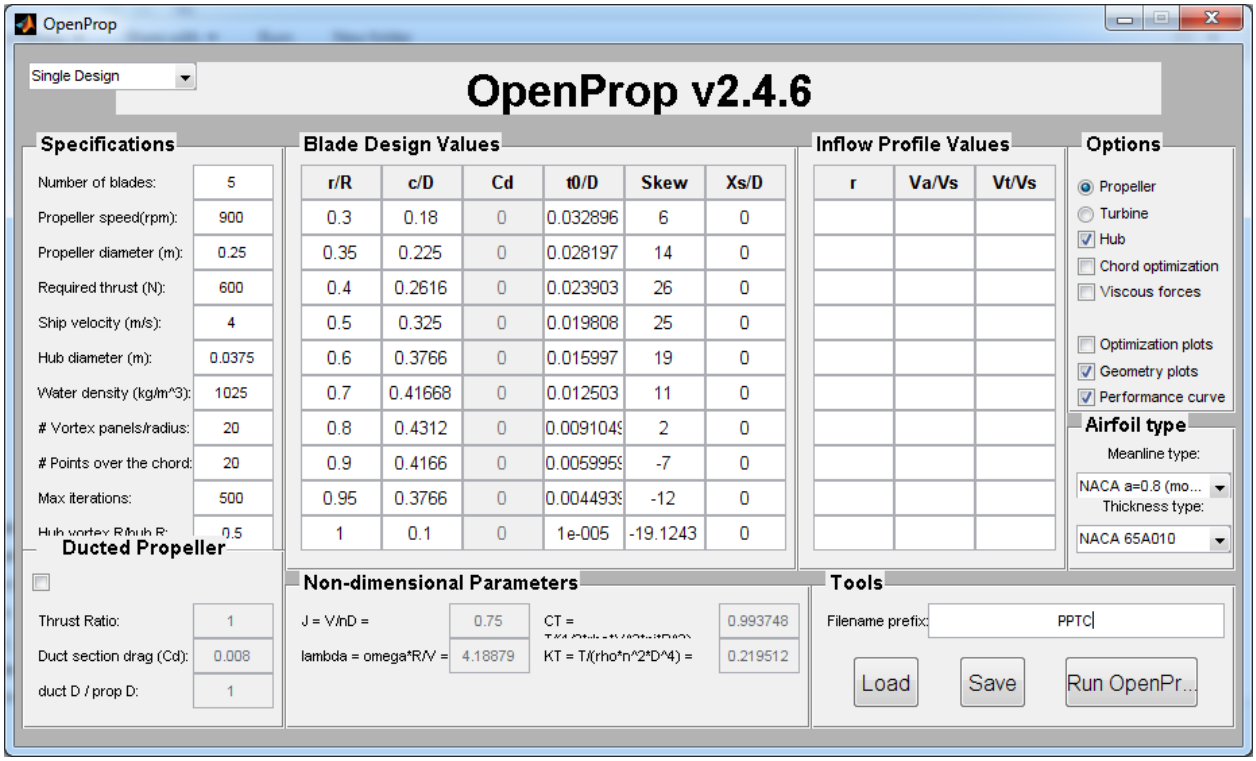

Figure 8 OpenProp v2.4.6 main window

In this application the propeller geometrical characteristics are introduced at each radius. It creates a simplified view of the propeller (Figure 9) by interpolating the input values. . In the input of the application a number of points, thru which the computation is carried out, is entered.

As mentioned in the above theory, the circulation (Figure 10) is computed at different radius of the blade. Considering the skew and the rake the incidence of the flow (Figure 11) is computed. According to the diagram in Figure 7 the velocity over the radius is determined (Figure 12).

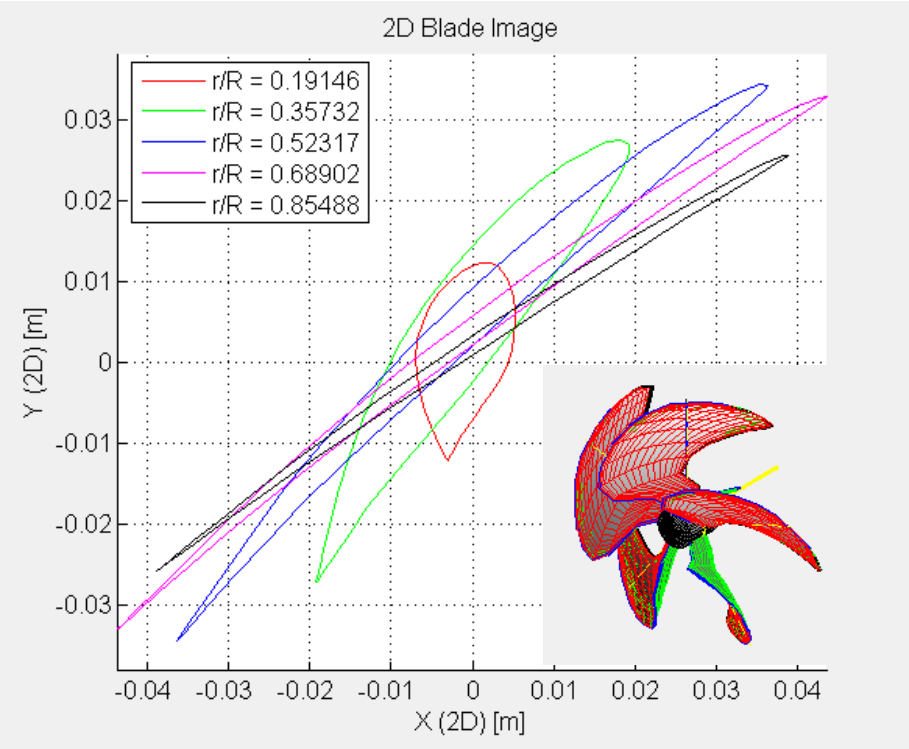

Figure 9 Geometrical representation 2D and 3D

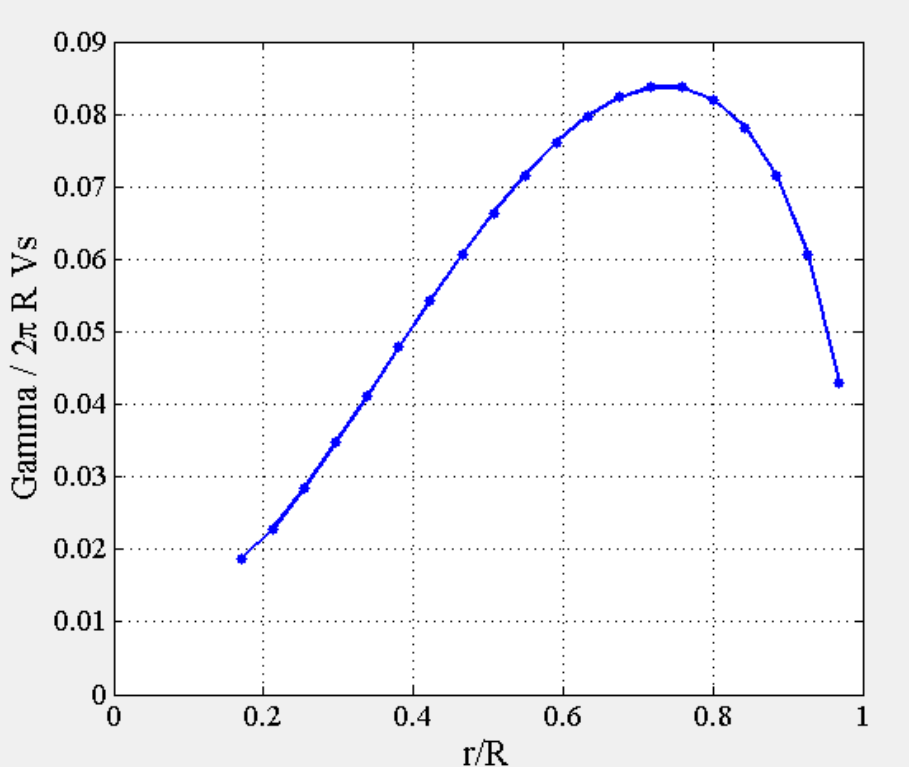

Figure 10 Distribution of the circulation over the radius

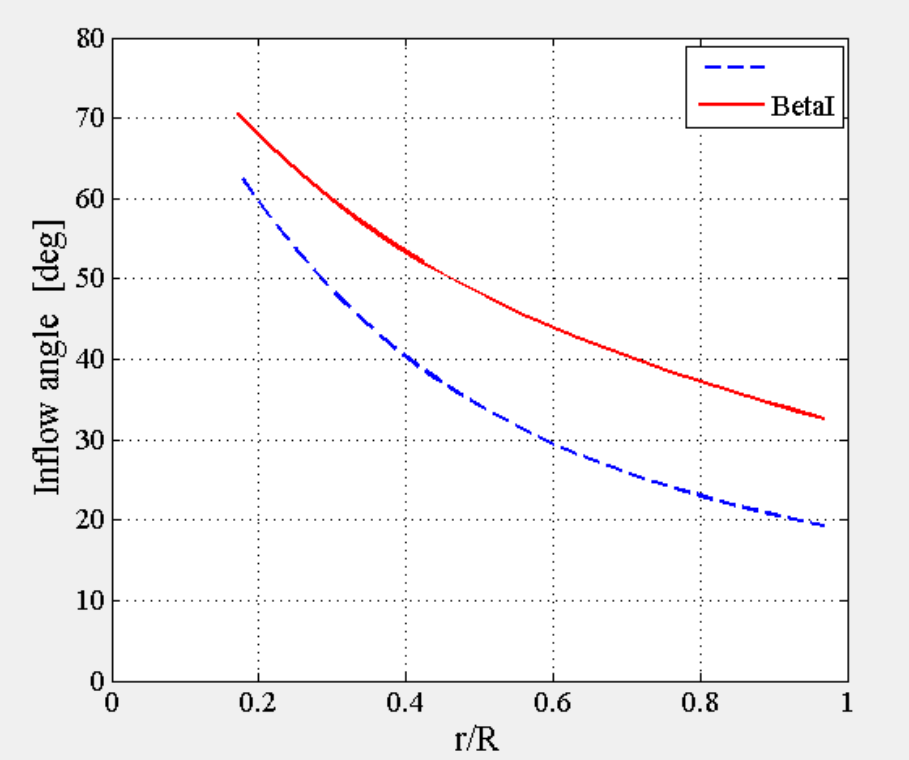

Figure 11 Advance angle over the radius

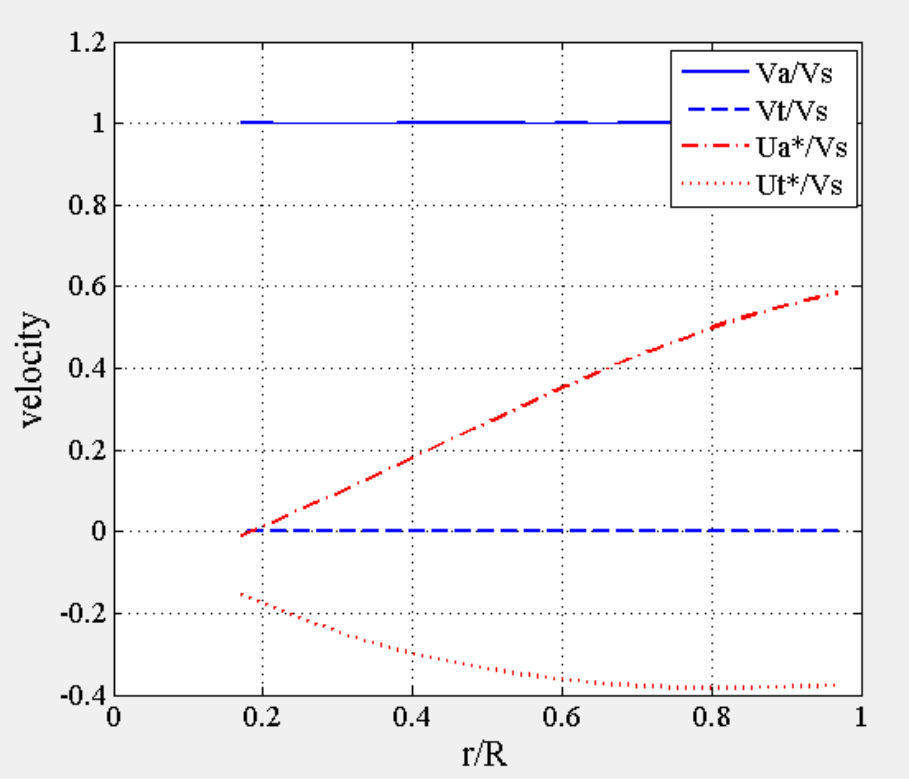

Figure 12 Velocity over the radius

Having the circulation and the velocity, the lift coefficient (Figure 13) is computed, after which the force and torque can be determined.

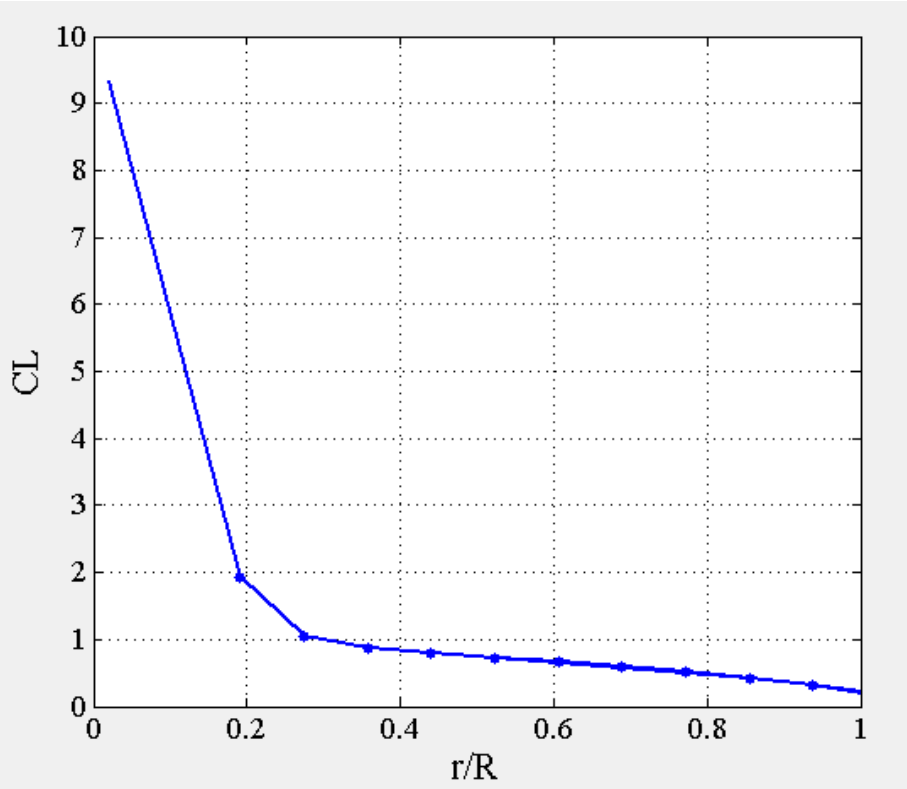

Figure 13 Lift coefficient over the radius

The thrust and torque coefficients as well as the efficiency of the propeller obtained as mentioned in Chapter 4 are presented in Table . The open water diagram is presented in Figure 14.

Table 3 Lifting line results

v [m/s]	J [-]	K_T [-]	K_Q [-]	η_0 [-]
2.25	0.6	0.85	0.227	0.357
2.625	0.7	0.816	0.222	0.408
3	0.8	0.777	0.217	0.454
3.375	0.9	0.737	0.211	0.498
3.75	1	0.694	0.204	0.541
4.125	1.1	0.651	0.195	0.582
4.5	1.2	0.606	0.186	0.622
4.875	1.3	0.558	0.175	0.66
5.25	1.4	0.507	0.162	0.696
5.625	1.5	0.454	0.148	0.728
6	1.6	0.398	0.134	0.756
6.375	1.7	0.339	0.117	0.779
6.75	1.8	0.278	0.1	0.793
7.125	1.9	0.215	0.082	0.791

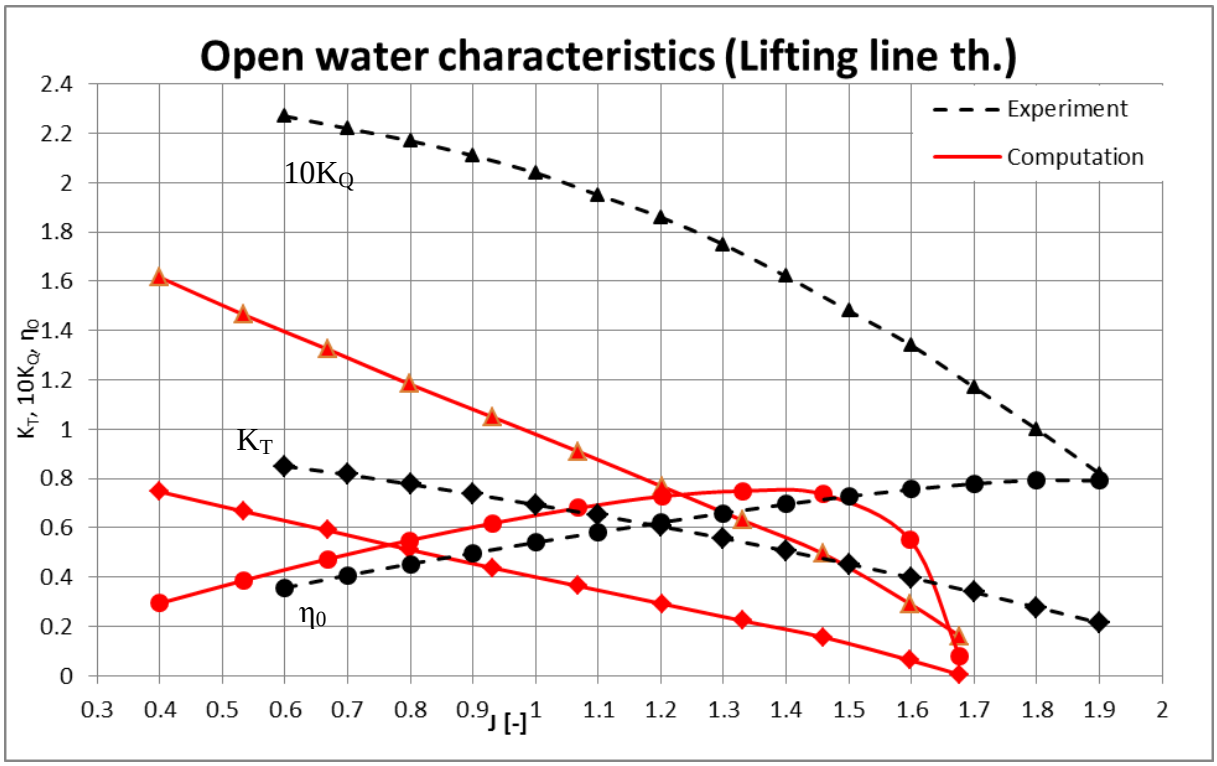

Figure 14 Open water diagram for lifting line method

We can observe that the thrust coefficient K_T and torque coefficient K_Q decrease when the advance coefficient J increases. On the other hand, the open water efficiency η_0 increases when J increases, however, the increase of J over 1.8 it slows it down. Therefore the highest efficiency is obtained at an advance ratio J of about 1.8.

Comparing the results obtained with the lifting line theory with the experimental results (see Appendix A4), it shows a big difference for thrust and torque coefficient. The efficiency is close to the experiment, until J=1.5, but the method fails in finding the maximum, as it can be seen from the graphic the maximum efficiency is obtained at J=1.8.

Further on, another method to compute the characteristics of the propeller is employed. This method is based on CFD computation, therefore in the following some basis on the methodology of this method will be presented before the actual simulation.

6. CONCEPTS OF FLUID MECHANICS

Applying the fundamental laws of mechanics to a fluid we obtain the governing equations for a fluid. The conservation of mass equation is:

$$\frac{\partial p}{\partial t} + \nabla \cdot \left(\rho \vec{V}\right) = 0 \tag{22}$$

and the conservation of momentum equation is:

$$\rho \frac{\partial \vec{V}}{\partial t} + \rho\left(\vec{V} \cdot \nabla\right)\vec{V} = -\nabla p + \rho \vec{g} + \nabla \cdot \tau_{ij} \tag{23}$$

These equations along with the conservation of energy equation form a set of coupled, non-linear partial differential equations. It is not possible to solve these equations analytically for most engineering problems.

However, it is possible to obtain approximate computer-based solutions to the governing equations for a variety of engineering problems.

Broadly, the strategy of CFD is to replace the continuous problem domain with a discrete domain using a grid. In the continuous domain, each flow variable is defined at every point in the domain. For instance, the pressure p in the continuous 1D domain shown in the figure below would be given as:

$$p = p(x),\ 0 < x < 1 \tag{24}$$

In the discrete domain, each flow variable is defined only at the grid points. So, in the discrete domain shown below, the pressure would be defined only at the N grid points.

$$p_i = p(x_i),\ i = 1, 2, \ldots, N \tag{25}$$

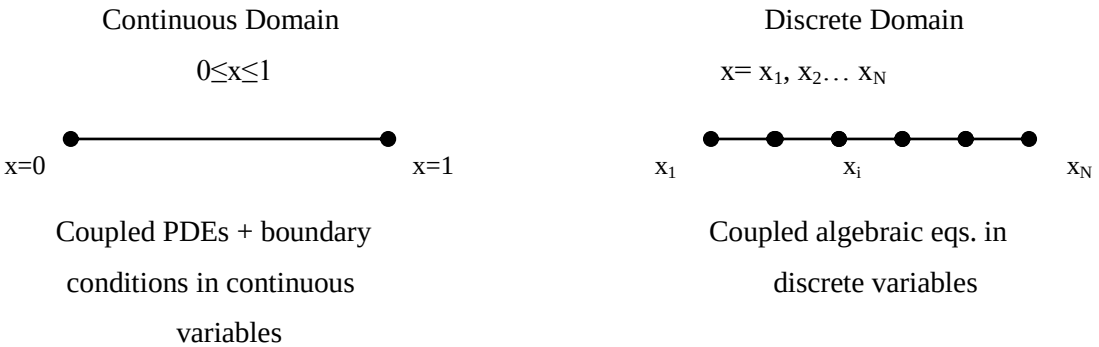

CFD comprises methods that solve the basic field equations subject to boundary conditions by approaches involving a large number of (mathematically simple) elements. These approaches lead automatically to a large number of unknowns. Unknowns which are obtained from the differential system of equations, used to discretize the continuous domain.

Basic CFD techniques, that require a grid to discretize the domain, are:

- Boundary element methods (BEM)
- Finite element methods (FEM)
- Finite difference methods (FDM)
- Finite volume methods (FVM)

Boundary element methods are used for potential flows, where the integrals over the whole fluid domain can be transformed to integrals over the boundaries of the fluid domain. The step from space (3-d) to surface (2-d) simplifies grid generation and often accelerates computations. Therefore practical applications for potential flows about ships (e.g. wave resistance problems) use exclusively BEM which are called panel methods. Panel methods divide the surface of a ship (and often part of the surrounding water surface) into discrete elements (panels). Each of these elements automatically fulfills the Laplace equation. Indirect methods determine the element strengths so that at the collocation points (usually centers of the panels) a linear boundary condition (e.g. zero normal velocity) is fulfilled. This involves the solution of a full system of linear equations with the source strengths as unknowns, after which the required velocities are computed, in a second step. Bernoulli's equation yields then the pressure field. Direct methods determine the potential directly. They are less suited for boundary conditions involving higher derivatives of the potential, but yield higher accuracy for lifting flows. Most of the commercially used codes for ship flows are based on indirect methods. BEM cannot be used to solve RANSE or Euler equations.

Finite element methods dominate structural analysis. For ship hydrodynamics they play only a minor role. Unlike in structural analysis, the elementary functions cannot be used also as weight functions to determine the weighted error integrals (residuals) in a Galerkin method. This reduces the elegance of the method considerably.

Finite difference methods discretize the whole fluid domain (just like FEM). The derivatives in the field equations are approximated by finite differences. Discretization errors can lead to a violation of conservation of mass or momentum. While FDM lose popularity and

finite volume methods (FVM) gain popularity, FDM gives in many cases results of comparable quality.

Finite volume methods also employ finite differences for the spatial and temporal discretization. However, they integrate the equations for mass and momentum conservation over the individual cell before variables are approximated by values at the cell center. This ensures conservativeness, i.e. mass and momentum are conserved because errors at the exit face of a cell cancel with errors at the entry face of the neighbor cell. Most commercial RANSE solvers today are based on FVM.

There are also mesh-less methods like:

- Smoothed particle hydrodynamics (SPH) (1977)
- Diffuse element method (DEM) (1922)
- Element-free Galerkin method (EFG/EFGM) (1994)
- Reproducing kernel particle method (RKPM) (1995)
- Finite pointset method (FPM) (1998)

A goal of mesh-less methods is to facilitate the simulation of increasingly demanding problems that require the ability to treat large deformations, advanced materials, complex geometry, nonlinear material behavior, discontinuities and singularities. For example the melting of a solid or the freezing process can be simulated using meshfree methods. There is also an additional 'sales' oriented aspect of this name. Mesh-less (or 'meshfree' as this is also used) methods seem attractive as alternative to the finite element method (FEM) for the general engineering community, which consider the process of generating finite element meshes as more difficult and expensive than the remainder of analysis process. Nevertheless these methods are still developing and require very strong computation power, which is why they are restricted to research field.

In a CFD solution, one would directly solve for the relevant flow variables only at the grid points. The values at other locations are determined by interpolating the values at the grid points.

The governing partial differential equations and boundary conditions are defined in terms of the continuous variables p, $\vec{V}$ etc. One can approximate these in the discrete domain in terms of the discrete variables p_i, $\vec{V}_i$ etc. The discrete system is a large set of coupled, algebraic equations in the discrete variables. Setting up the discrete system and solving it (which is a matrix inversion problem) involves a very large number of repetitive calculations.

There are two radically different states of flows that are easily identified and distinguished: laminar flow and turbulent flow. Laminar flows are characterized by smoothly varying velocity fields in space and time in which individual sheets move past one another without generating cross currents. These flows arise when the fluid viscosity is sufficiently large to damp out any perturbations to the flow that may occur due to boundary imperfections or other irregularities. These flows occur at low-to-moderate values of the Reynolds number. In contrast, turbulent flows are characterized by large, nearly random fluctuations in velocity and pressure in both space and time. These fluctuations arise from instabilities that grow until nonlinear interactions cause them to break down into finer and finer whirls that eventually are dissipated (into heat) by the action of viscosity [16].

The equations governing a turbulent flow are more or less the same as for a laminar flow; however, the solution is clearly much more complicated in this regime. The approaches on solving the flow equations for a turbulent flow field can be roughly divided into two classes. Direct numerical simulations (DNS) use the speed of modern computers to numerically integrate the Navier Stokes equations, resolving all of the spatial and temporal fluctuations, without resorting to modeling. In essence, the solution procedure is the same as for laminar flow, except the equations must deal with resolving all of the fluctuations in the velocity and pressure. DNS remains limited to very simple geometries (e.g., channel flows, jets and boundary layers) and is extremely expensive to run. The alternative to DNS found in most CFD packages (including FLUENT) is to solve the Reynolds Averaged Navier Stokes (RANS) equations. RANS equations govern the mean velocity and pressure. Because these quantities vary smoothly in space and time, they are much easier to solve; however, as will be shown below, they require modeling to “close” the equations and these models introduce significant error into the calculation.

6.1 Reynolds Averaged Navier-Stokes

Hence DNS is very difficult to perform; we are forced to account for the effects of turbulence in an approximate manner. For this purpose, a large variety of turbulence models were developed and the research still goes on. There are five principal classes of turbulence models [16]:

i. algebraic,
ii. one-equation,
iii. multiple-equation,

iv. second-order closures (Reynolds-stress models),

v. Large-Eddy Simulation (LES).

The first approach for the approximate treatment of turbulent flows was presented by Reynolds in 1895. The methodology is based on the decomposition of the flow variables into a mean and a fluctuating part.

Considering an incompressible flow, in the governing equations (26), the velocity components and the pressure are substituted by (27), and then solved for the mean values.

$$\begin{gathered}\frac{\partial V_k}{\partial x_k}=0\\ \frac{\partial V_i}{\partial t}+\frac{\partial V_i}{\partial x_k}V_k=-\frac{1}{\rho}\frac{\partial P}{\partial x_i}+\frac{\mu}{\rho}\left(\frac{\partial^2 V_i}{\partial x_k \partial x_k}\right)+f_i\end{gathered} \tag{26}$$

$$\begin{gathered}V_i=\overline{V}_i+V_i'\\ P=\overline{P}+P'\end{gathered} \tag{27}$$

In the above equation the mean value is denoted by an over bar and the turbulent fluctuations by a prime. The mean values are obtained by an averaging procedure [16]. There are three different forms of the Reynolds averaging:

1. Time
2. Spatial
3. Ensemble

In cases where the turbulent flow is both stationary and homogeneous, all three averaging forms are equivalent [5].

If we apply either the time averaging or the ensemble averaging to the incompressible Navier-Stokes equations we obtain the following relations for the mass and momentum conservation:

$$\begin{gathered}\frac{\partial \overline{V}_k}{\partial x_k}=0\\ \frac{\partial \overline{V}_i}{\partial t}+\frac{\partial \overline{V}_i}{\partial x_k}\overline{V}_k=-\frac{1}{\rho}\frac{\partial \overline{P}}{\partial x_i}+\frac{\partial \overline{\tilde{V}_i \tilde{V}_k}}{\partial x_k}+\frac{\mu}{\rho}\left(\frac{\partial^2 \overline{V}_i}{\partial x_k \partial x_k}\right)+f_i\end{gathered} \tag{28}$$

These are known as the Reynolds-Averaged Navier Stokes equations (RANS). The equations (28) are formally identical to the Navier-Stokes equations (26) with the exception of the additional term (29), entitled Reynolds stress tensor.

$$R_{ij} = -\rho\overline{\tilde{V}_i \tilde{V}_k} \tag{29}$$

This tensor represents the transfer of momentum due to turbulent fluctuations and it consists, in 3D, in nine components:

$$\overline{\rho\tilde{V}_i \tilde{V}_j} = \begin{bmatrix} \overline{\rho\tilde{V}_1^{\,2}} & \overline{\rho\tilde{V}_1 \tilde{V}_2} & \overline{\rho\tilde{V}_1 \tilde{V}_3} \\ \overline{\rho\tilde{V}_2 \tilde{V}_1} & \overline{\rho\tilde{V}_2^{\,2}} & \overline{\rho\tilde{V}_2 \tilde{V}_3} \\ \overline{\rho\tilde{V}_3 \tilde{V}_1} & \overline{\rho\tilde{V}_3 \tilde{V}_2} & \overline{\rho\tilde{V}^{2}_{3}} \end{bmatrix} \tag{30}$$

Since $\tilde{V}_i$ and $\tilde{V}_j$ in the correlations can be interchanged, the Reynolds-stress tensor contains only six independent components. The sum of the normal stresses divided by density defines the turbulence kinetic energy:

$$K = \frac{1}{2}\overline{\tilde{V}_i \tilde{V}_k} = \frac{1}{2}\left[\overline{\tilde{V}_1^{\,2}} + \overline{\tilde{V}_2^{\,2}} + \overline{\tilde{V}_3^{\,2}}\right] \tag{31}$$

6.2 Turbulence model

6.2.1 The k-ω model

As it was showed above, the fundamental problem of turbulence modeling, based on the Reynolds-averaged Navier-Stokes equations, is to find six additional relations in order to close the system of equations.

There are various models (about 200) to simulate the eddy viscosity. They are classified in terms of transport equations solved in addition to the RANS equations:

a) zero-equation/algebraic models: Mixing Length, Cebeci-Smith, Baldwin-Lomax, etc.;
b) one-equation models: Wolfstein, Baldwin-Barth, Spalart-Allmaras, k-model, etc.;
c) tow-equation models: k-ε, k-ω, k-τ, k-L, etc.;
d) three-equation models: k-ε-A, etc.;
e) four-equation models: v^2-f, etc.

Turbulence modeling is a rather broad discipline and an in-depth discussion is beyond the scope of this paper. The k- ε turbulence model is the most widely employed two-equation eddy viscosity model, here we simply note that the Reynolds stress is modeled in terms of two turbulence parameters, the turbulent kinetic energy *k* and the turbulent energy dissipation rate ε defined below:

$$k = \frac{1}{2}\left(\overline{u'^2} + \overline{v'^2} + \overline{w'^2}\right)$$

$$\varepsilon = \nu\left[\left(\frac{\partial u'}{\partial x}\right)^2 + \left(\frac{\partial u'}{\partial y}\right)^2 + \left(\frac{\partial u'}{\partial z}\right)^2 + \left(\frac{\partial v'}{\partial x}\right)^2 + \left(\frac{\partial v'}{\partial y}\right)^2 + \left(\frac{\partial v'}{\partial z}\right)^2 + \left(\frac{\partial w'}{\partial x}\right)^2 + \left(\frac{\partial w'}{\partial y}\right)^2 + \left(\frac{\partial w'}{\partial z}\right)^2\right] \quad (32)$$

The k-ε turbulence model requires addition of the so-called damping functions in order to stay valid through the viscous sub-layer to the wall. The aim of the damping functions is to assure proper limiting behavior of *k* and ε at the wall.

$$\frac{\varepsilon}{k} \sim \frac{2\nu}{y^2}, \quad \text{for} \quad y \to 0 \quad (33)$$

,where *y* represents the coordinate normal to the wall.

The *k*-ε models with damping functions are also denoted as low Reynolds number models. The damping functions lead to turbulence equations with stiff source terms. This, and the necessary high grid resolution nearby walls (in order to resolve the viscous sub-layer), requires the utilization of at least point-implicit or better full-implicit time-stepping schemes [5], which are known to be unconditionally stable [13] for steady flows.

6.2.2 The Spalart-Allmaras model

Spalart-Allmaras model is a one equation model which solves the transport equation. In the final form of the model there have been introduced two variables $\tilde{\nu}$, which is equal to ν_t except in the viscous range, and $X \equiv \tilde{\nu}/\upsilon$. By choosing a transported quantity $\tilde{\nu}$ is in the benefit of the numerical solution, because this is easier to solve than *U*, in contrast with other variables like dissipation rate ε or turbulent kinetic energy *k*, mentioned above. Therefore using Spalart-Allmaras model doesn't require a finer grid compared to *k*-ε or *k*-ω.

The reason that $\tilde{\nu}$ variable has been introduced is that eddy viscosity ν_t equals with kyu_T in the log layer (Figure 15) but not in the buffer layer of the turbulence. Therefore $\tilde{\nu}$ was defined so that equals kyu_T all the way to the wall, which leads to the following equations:

$$\nu_t = \tilde{\nu} * f_{\nu 1} \tag{34}$$

$$f_{\nu 1} = \frac{X^3}{X^3 + c_{\nu 1}^3} \tag{35}$$

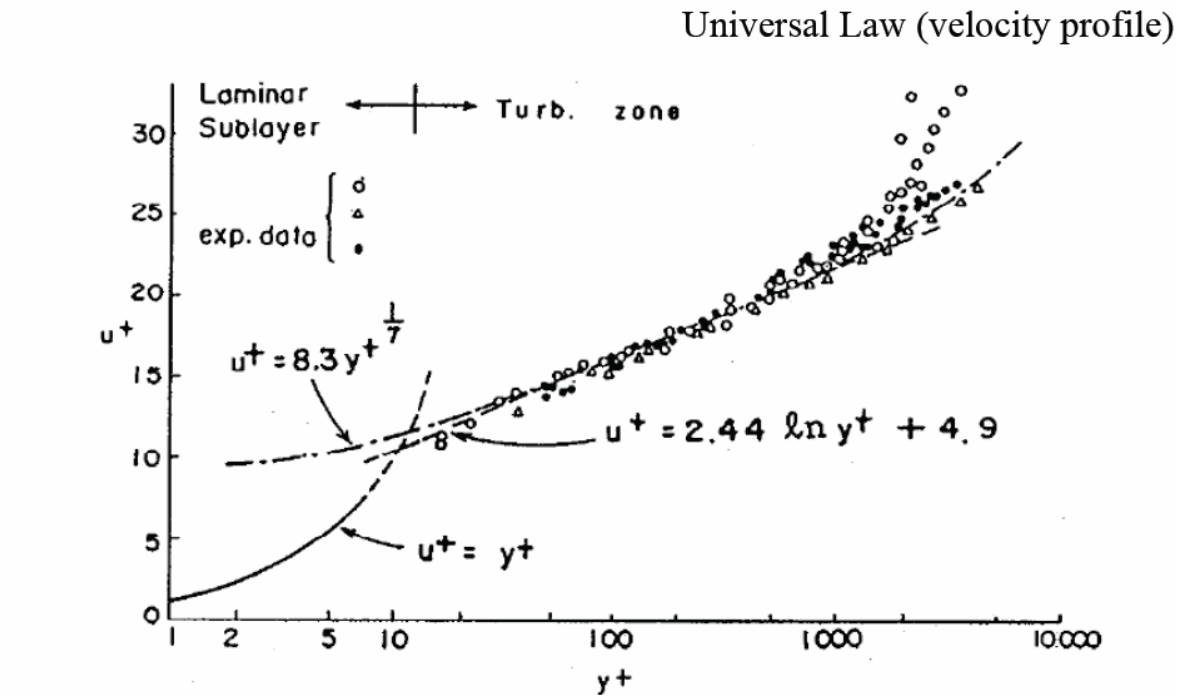

Figure 15 Turbulent boundary layer

After numerically modeling the so called diffusion, production and destruction terms in the transport equation (26), and calibrate the constants that take part in the equations the final form of the model is obtained.

$$\frac{D\tilde{\nu}}{Dt} = c_{b1}\tilde{S}\tilde{\nu} + \frac{1}{\sigma}\left[\nabla\cdot\left((\nu+\tilde{\nu})\nabla\tilde{\nu}\right) + c_{b2}\left(\nabla\tilde{\nu}\right)^2\right] - c_{w1} f_w \left[\frac{\tilde{\nu}}{d}\right]^2 \tag{36}$$

6.3 Numerical Stability

As mentioned above, in order to compute the flow, it is necessary to discretize the domain of the fluid. Considering the discretization using cells like in Figure 16, and applying the integral form of the continuity equation (37) for steady, incompressible flow we obtain the discrete form of the continuity equation for a cell (38).

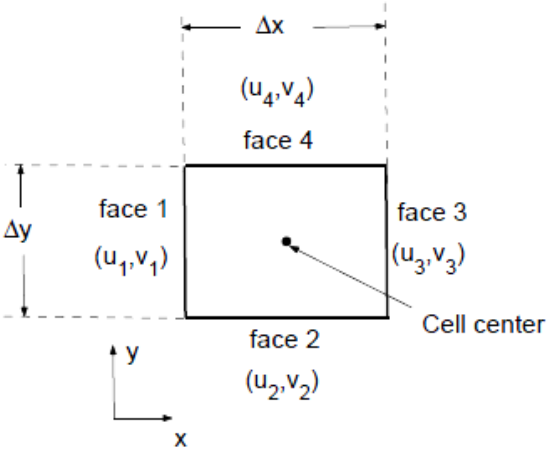

Figure 16 Cell configuration

$$\int_S \vec{V} \cdot \hat{n} dS = 0 \tag{37}$$

$$-u_1 \Delta y - v_2 \Delta x + u_3 \Delta y + v_4 \Delta x = 0 \tag{38}$$

Applying the above equations to all the cells in the domain and assembling them we obtain a discrete system of equations.

The momentum conservation equation (28) for a fluid is nonlinear due to the convection term $(\vec{V} \cdot \nabla)\vec{V}$. Phenomena such as turbulence introduce additional nonlinearities. The highly nonlinear nature of the governing equations for a fluid makes it challenging to obtain accurate numerical solutions for complex flows of practical interest.

Therefore to eliminate the nonlinearities it is necessary to linearize the equations about a guess value of the solution and to iterate until the guess agrees with the solution to a specified tolerance level.

In order to obtain the numerical solution of the discrete system of equations we must use an implicit or explicit method.

Explicit methods calculate the state of a system at a later time from the state of the system at the current time, while implicit methods find a solution by solving an equation involving both the current state of the system and the later one. It is obvious that to solve the

equations in two states of the system, meaning to use the implicit scheme, will take more computational time, but the errors will be damped out irrespective of how large the time step is, because the values for all the points in the grid are calculated simultaneously.

In contrast with the implicit scheme, the explicit one is easier to implement, but the solution of the system may not converge due to the nature of the scheme.

6.4 Basic CFD steps

The field of computational fluid dynamics has a broad range of applicability. Independent of the specific application under study, the following sequence of steps generally must be followed in order to obtain a satisfactory solution.

A. Approximation of the geometry.

The geometry of the physical system needs to be approximated by a geometric CAD type model. The more closely the model geometry represents the actual geometry, the more accurate the results are likely to be.

B. Creation of the numerical grid within the geometrical model.

To identify the discrete, finite locations at which the variables are to be calculated, the geometry is divided into a finite number of cells that make up the numerical grid. Before doing this, it is necessary to identify the physical flow phenomena expected (turbulence, compressible flow, shocks, combustion, multiphase flow, mixing, etc.) so the grid generated is suitable to capture these phenomena.

C. Selection of models and modeling parameters.

Once the geometry and grid have been established, the mathematical models and parameters for those phenomena are then selected and boundary conditions defined throughout the domain.

D. Calculation of the variable values.

Discretization yields a large number of algebraic equations (one set for each cell). These equations are then generally solved using an iterative method, starting with a first guess value for all variables and completing a computational cycle. Error or residual values are computed from the discretized equations and the calculations repeated many times, reducing the residual values, until a sufficiently converged solution is judged to have been reached.

E. Determination of a sufficiently converged solution.

The final stage in the solution process is to determine when the solution has reached a sufficient level of convergence. When the sum of the residual values around the system becomes sufficiently small, the calculations are stopped and the solution is considered converged. A further check is that additional iterations produce negligible changes in the variable values.

F. Post Processing.

Once a converged solution has been calculated, the results can be presented as numerical values or pictures, such as velocity vectors and contours of constant values (e.g. pressure or velocity).

G. Solution Verification and Validation

Once the solution process is complete, each solution should be verified and validated. If this cannot be completed successfully, re-simulation may be required, with different assumptions and / or improvements to the grid, models and boundary conditions used.

7. GEOMETRY MODEL AND MESH GENERATION

Due to the steadily increasing demands on the complexity and fidelity of flow simulations, grid generation methods had to become more and more sophisticated. The development started first with relatively simple structured meshes constructed either by algebraic methods or by using partial differential equations. But with increasing geometrical complexity of the configurations, the grids had to be broken into a number of topologically simpler blocks (multiblock approach).

The next logical step was to allow for non-matching interfaces between the grid blocks in order to relieve the constraints put on the grid generation in a single block. Finally, solution methodologies were introduced which can deal with grids overlapping each other (Chimera technique).

However, the generation of a structured, multiblock grid for a complicated geometry may still take weeks to accomplish. Therefore, the research also focused on the development of unstructured grid generators (and flow solvers), which promise significantly reduced setup times, with only a minor user intervention. Another very important feature of the unstructured methodology is the possibility of solution based grid adaptation. The first unstructured grids consisted exclusively of isotropic tetrahedral, which was fully sufficient for inviscid flows governed by the Euler equations.

Nevertheless, the solution of the Navier-Stokes equations requires higher Reynolds numbers grids, which are highly stretched in the shear layers. Although such grids can also be constructed from tetrahedral elements, it is advisable to use prisms or hexahedra in the viscous flow regions and tetrahedral outside. This not only improves the solution accuracy, but it also saves the number of elements, faces and edges. Thus, the memory and run-time requirements of the simulation are reduced. In fact, today there is a very strong interest in unstructured, mixed-element grids and the corresponding flow solvers.

Finite element mesh design is a vital part of flow modeling. It is the most complex and time-consuming task in this process and to a large extent it determines the correctness of the results. The finite element mesh design problem can be approached in two ways:

- methodically – knowing the character of the flow one can try to generate a structural mesh whose shape matches that of the flow,
- by force – by applying, without any reservations, a non-structural mesh with a large number of elements.

The first approach is justified in cases when the geometry of the investigated flow is simple and there is no problem with properly arranging the elements. In the case of more complex phenomena, such as the flow around a screw propeller with high skew, it may turn out to be impossible to generate a proper structural mesh.

Many researchers incline to perform computations using a tetragonal non-structural mesh. This solution has many advantages: firstly, it is a very simple way of generating such meshes and it can be automated by scripting and secondly, the results are characterized by a very small error whereby entire screw propeller-hull and propeller-nozzle assemblies, tandem arrangements and so on can be analyzed. Additionally, in order to improve analytical results the boundary layer can be modeled by prismatic elements.

When modeling an isolated propeller it is best to assume the largest possible calculation domain. But one should note that the larger the domain, the greater the number of mesh elements. As the number of mesh elements increases so does the computing time. On the other hand, thanks to a larger domain convergent and correct results are obtained faster. The best solution is a compromise between the domain size and the number of elements.

8. SIMULATION SETUP

In the following the steps presented in Chapter 6 are being developed and applied to the actual problem.

A. Approximation of the geometry.

In the open water analyses the propeller is operated in a pull configuration, i.e. the shaft is located behind the propeller. The blades, hub, cap, and shaft are modeled according to the IGES-geometry file provided to the workshop participants.

The calculation domain is, in first calculations, a cylinder (Figure 17) having the inlet located five propeller diameters upstream from the propeller plane. The outlet is located ten propeller diameters downstream from the propeller plane. The outer side of the domain has radius of five propeller diameters. The sides of the calculation domain are located far from the propeller so that the effect of the boundaries is negligible in the simulations.

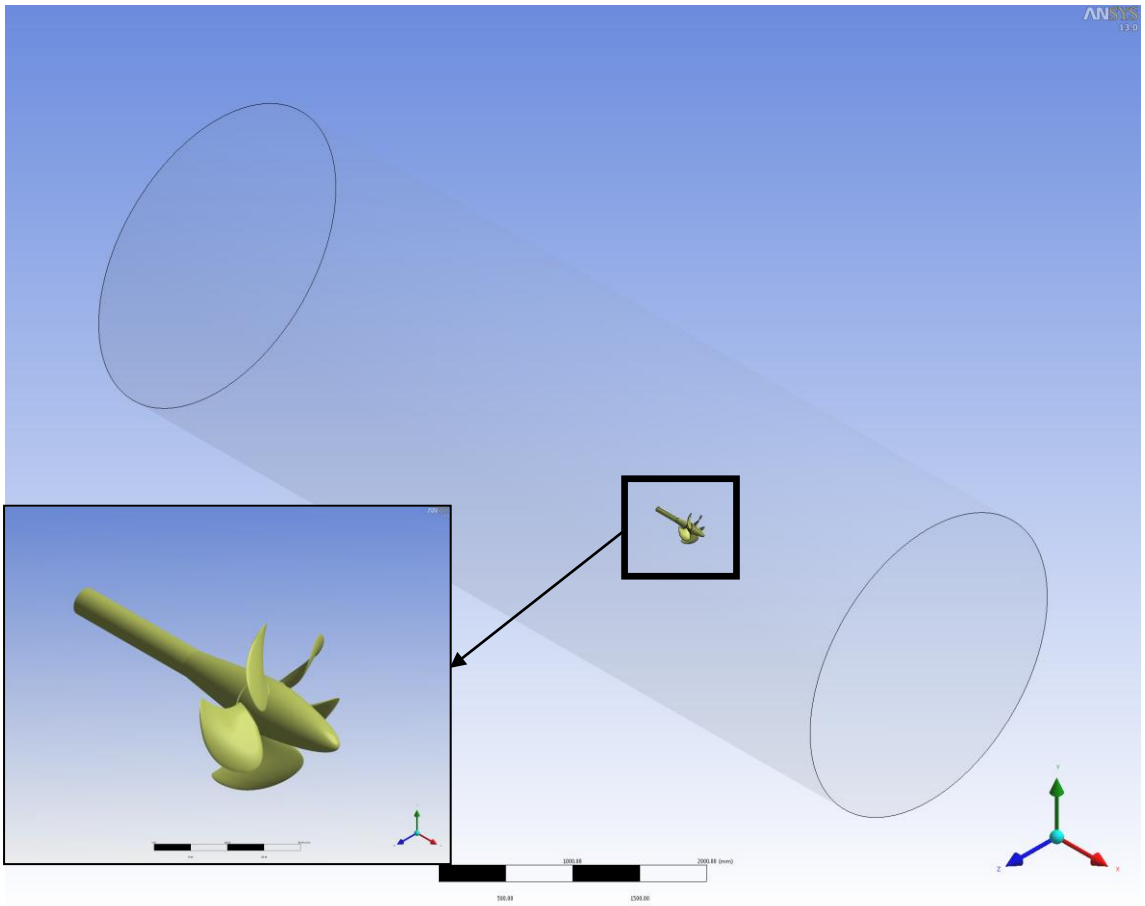

Figure 17 Computation domain (first case)

Hence computations showed considerable differences compared with the experiments, a new domain has been used in order to increase the cell number close to the propeller, which will give for the same computation time better accuracy. The second domain used (Figure 18)

is one fifth of the full cylinder due to the symmetry of the five bladed propeller. For propellers operating in a uniform inflow, periodic boundary conditions can be utilized in the circumferential direction. A blade passage with 72° periodicity in the circumferential direction constitutes the computational domain for the second case.

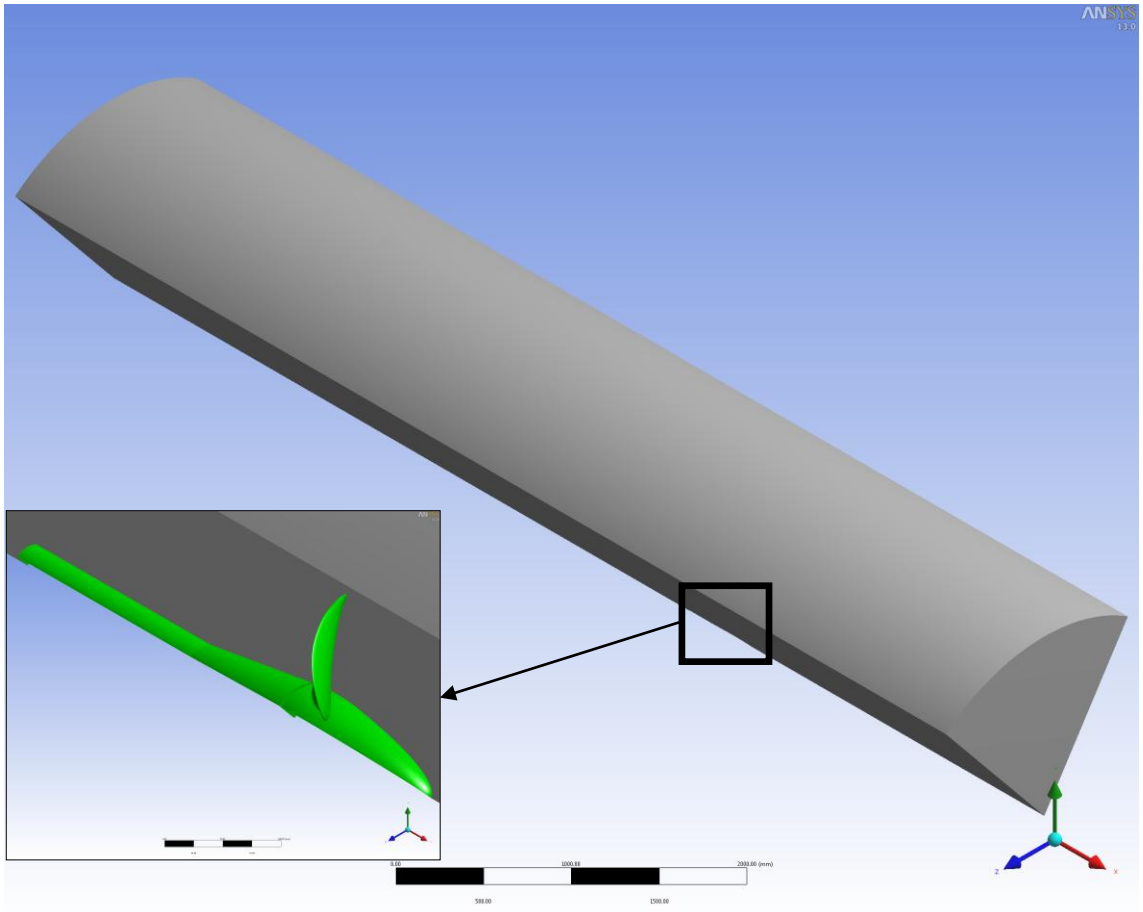

Figure 18 Computation domain (second case)

For both cases the coordinate system is such that the x-axis points to upstream direction, z-axis points upwards, and y-axis forms a right-handed coordinate system with the other axes. The right-handed propeller rotates in negative angular direction θ (see APPENDIX A2), i.e. θ is positive in left-handed direction in the propeller coordinate system.

B. Creation of the numerical grid within the geometrical model.

A tetrahedral mesh was generated inside each of the domain. First, the surfaces of the propeller and the boundaries of the domain were meshed with triangles (Figure 19 and Figure 20), using different functions to ensure higher quality next to the blade and hub of the propeller and coarser cells close to the boundaries (Figure 21 and Figure 22).

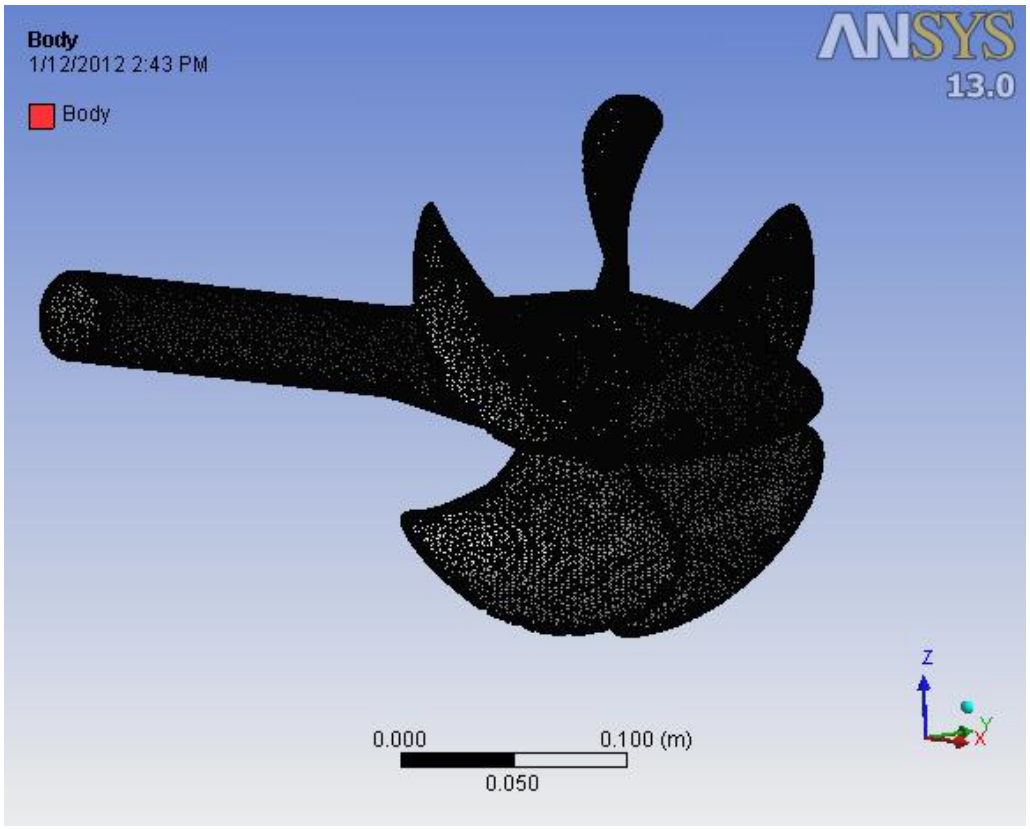

Figure 19 Meshed surfaces of blades, hub and boss (first case)

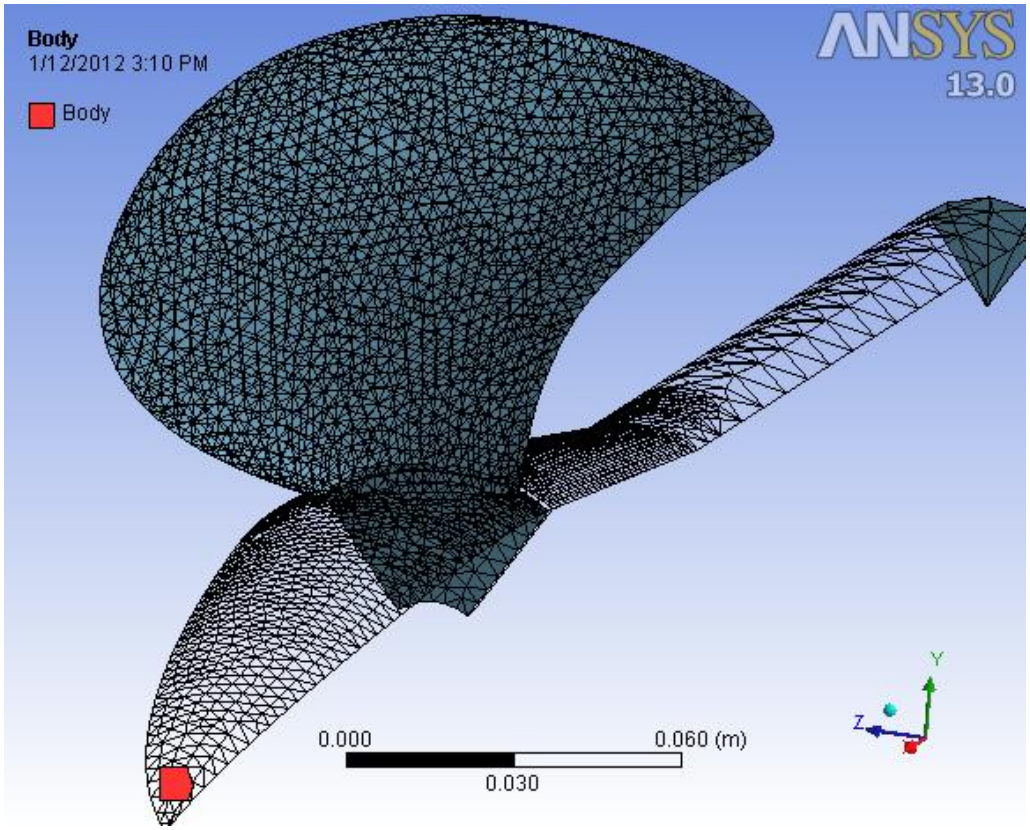

Figure 20 Meshed surfaces of the blade, hub and boss (second case)

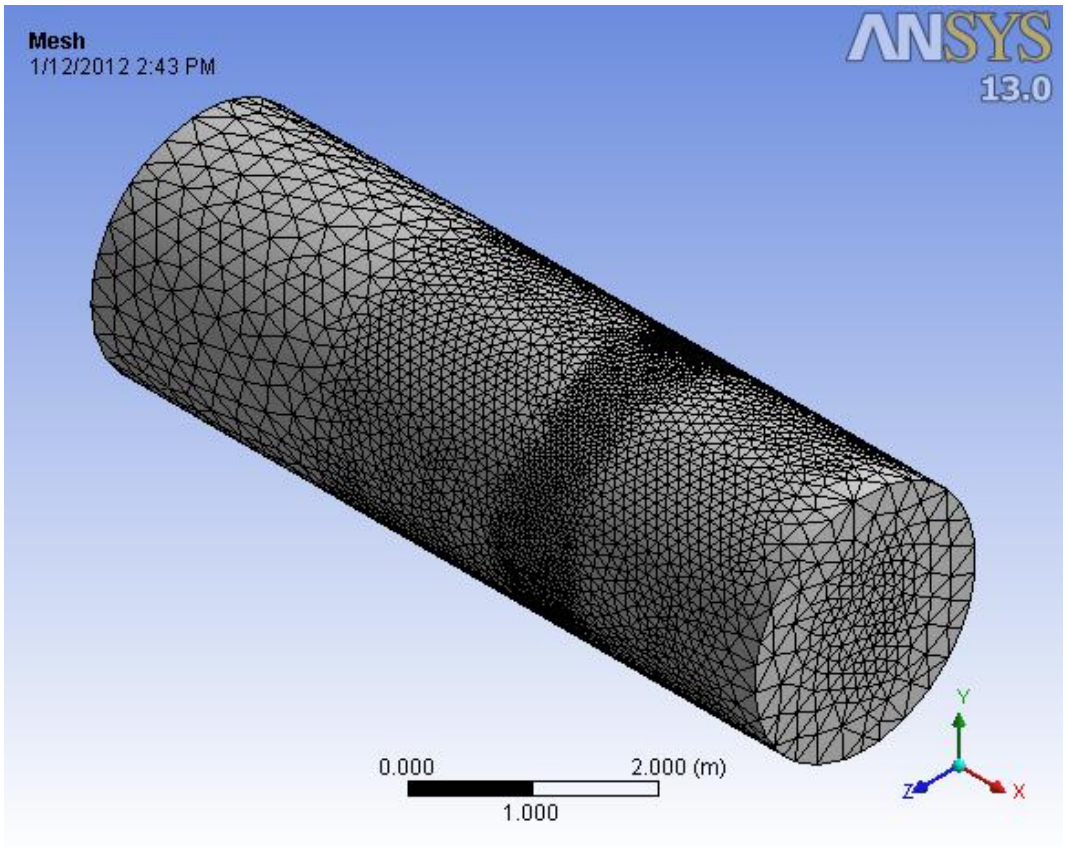

Figure 21 Meshed boundary of the domain (first case)

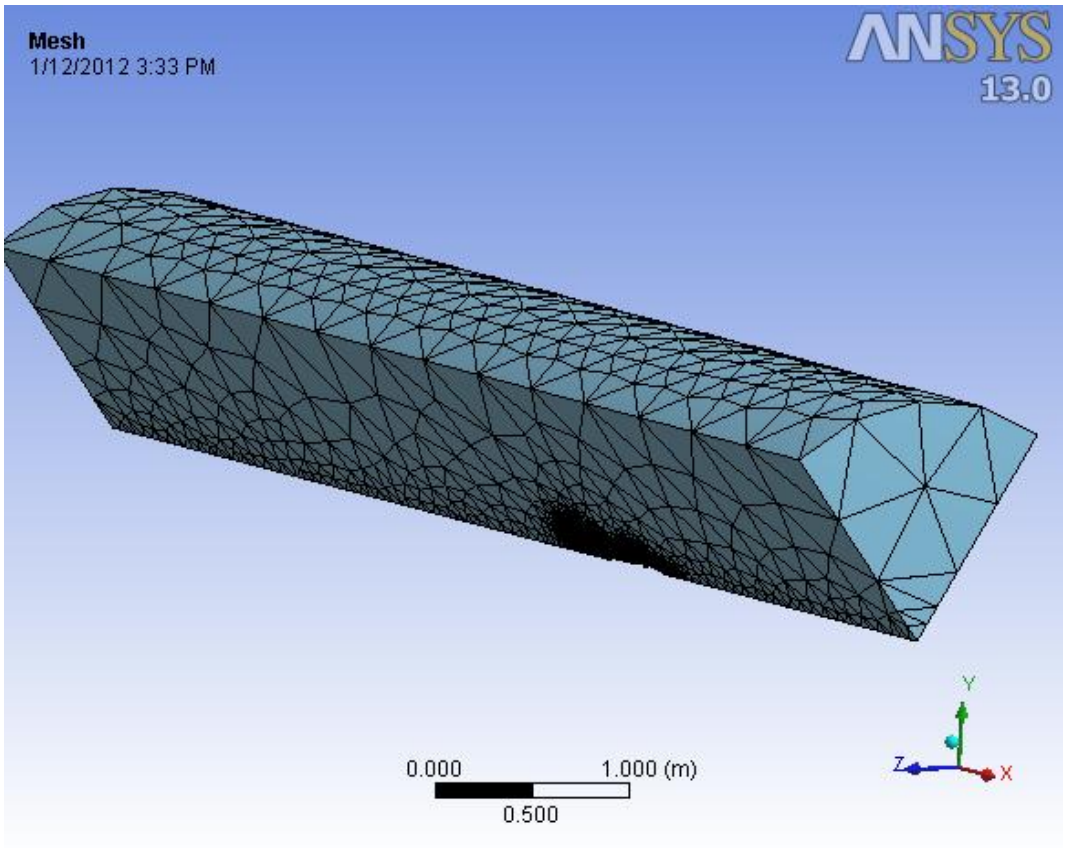

Figure 22 Meshed boundary of the domain (second case)

Furthermore the interior of the domain was meshed (Figure 23 and Figure 24) using tetrahedral elements, in the first case the model contained approximately 4 million cells, while the second one has about 2 million cells. A special attention has been paid to the area around the propeller as it can be seen in the details.

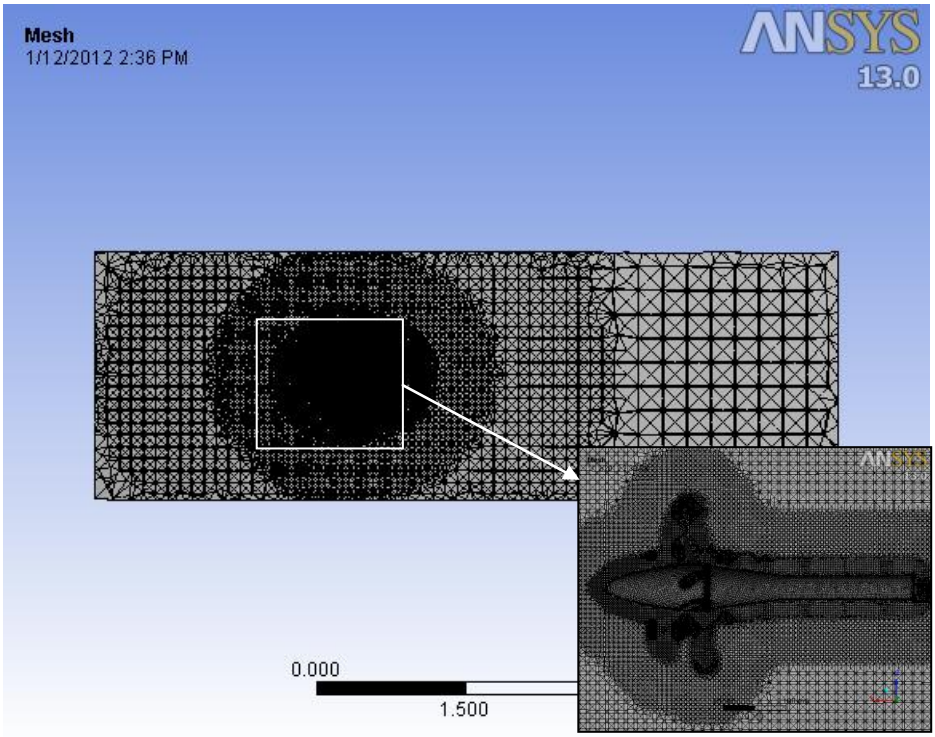

Figure 23 Section thru meshed interior of the domain (first case)

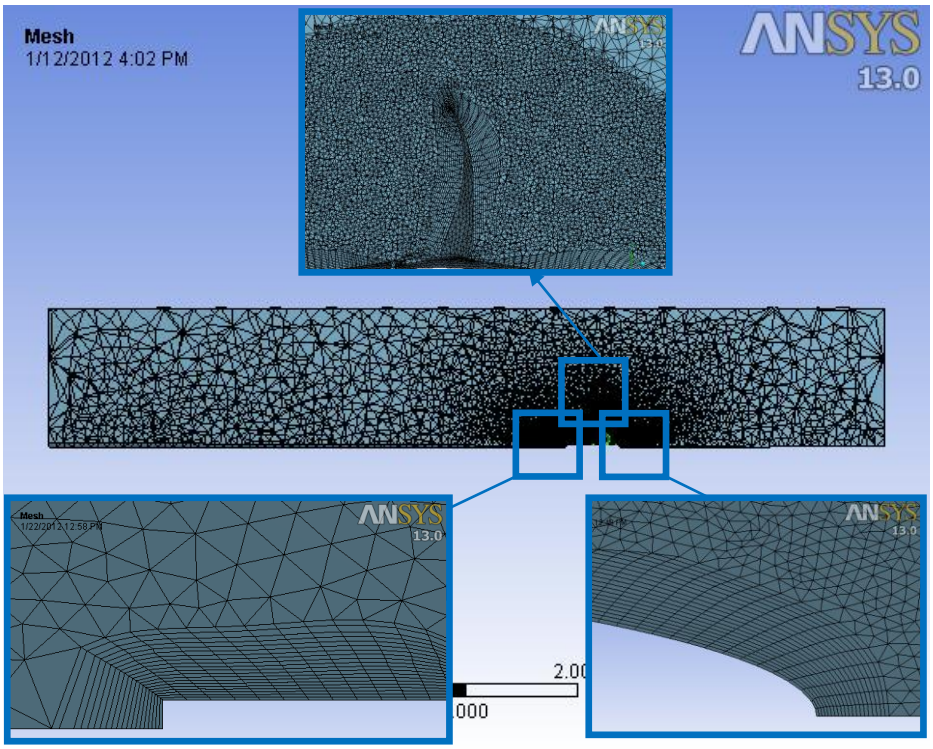

Figure 24 Section thru meshed interior of the domain (second case)

C. Selection of models and modeling parameters.

Even from the beginning of the simulation the FLUENT software offers to perform the calculation using single-precision or double precision. This last option is used when mean pressure levels in all but one of the zones can be quite large than the others, which is our case. Also when there are high-aspect-ratio grids the convergence or the accuracy can be affected due to inefficient transfer of boundary information. To avoid any of the above problems, the double-precision solver is chosen for the computation.

The assumptions that the fluid is incompressible and Newtonian allow for simplification of the fundamental equations for hydrodynamic applications. So the continuity equation and the subsequent conservation-of-momentum equations are all that are required in order to solve for the velocity and pressure fields of an incompressible flow.

The choice of turbulence model depends on considerations such as the physics encompassed in the flow, the level of accuracy required, the available computational resources and the amount of time available for the simulation. As mentioned in Chapter 6 initially was used a realizable k-ε model for the first computation, where the domain is a cylinder, and Spalart-Allmaras for the second computation. It has been chosen this model because is effectively a low-Reynolds-number model, requiring the viscous-affected region of the boundary layer to be properly resolved, and because in FLUENT, the Spalart-Allmaras model has been implemented to use wall functions when the mesh resolution is not sufficiently fine. This makes it a good choice for relatively crude simulations on coarse meshes. Furthermore, the near-wall gradients of the transported variable in the model are much smaller than the gradients of the transported variables in the k-ε or k-ω models. This makes the model less sensitive to numerical error when non-layered meshes are used near walls.

In order to reproduce the experiment as much as possible, the environmental conditions in which the experiment has been conducted (see Appendix A4) are adopted in the simulation.

The boundary conditions of the model are presented in Figure 25. For every case the upstream boundary has been defined as velocity-inlet, having different magnitudes for the velocity in X direction, starting from 1.5 [m/s] to 6 [m/s] with a step of 0.5. The downstream is considered as pressure outlet. For the domain modeled as a full cylinder, and as well for the second domain the surface of the cylinder is set as symmetry, due to the fact that the propeller

model is situated far enough from it and also to avoid supplementary wall conditions. For the propeller blades, hub and cap a no-slip wall condition has been used.

A special boundary condition is put on the second domain where the cuts are performed. These are rotational periodic boundary condition and are used when the physical geometry of interest and the expected pattern of the flow solution have a periodically repeating nature, which is the case of the propeller. FLUENT treats the flow at a periodic boundary as though the opposing periodic plane is a direct neighbor to the cells adjacent to the first periodic boundary. Therefore the plane close to the trailing edge is considered to be the neighbor of the plane close to the leading edge. Thus, when calculating the flow through the periodic boundary (incoming) adjacent to a fluid cell, the flow conditions at the fluid cell adjacent to the opposite periodic plane (outgoing) are used.

In order simulate the rotating movement of the propeller; a moving reference frame has been setup. When the moving reference frame is activated, the equations of motion are modified to incorporate the additional acceleration terms which occur due to the transformation from the stationary to the moving reference frame. By solving these equations in a steady-state manner, the flow around the moving parts can be modeled. Therefore the domain is supposed to rotate around X axis, with a revolution rate of 15 [s^{-1}].

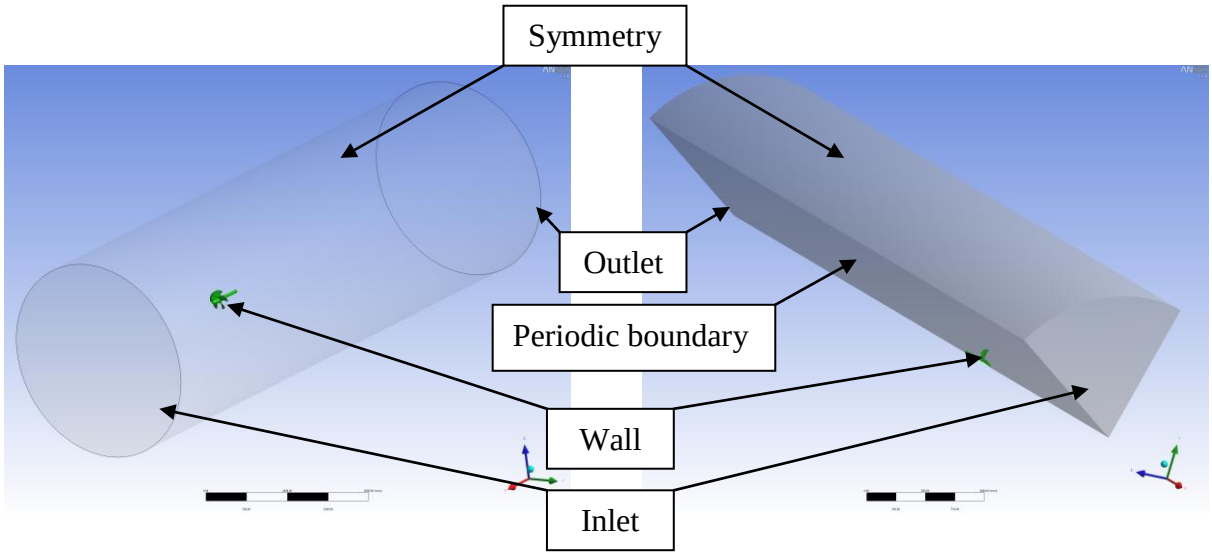

Figure 25 Boundary conditions

D. Calculation of the variable values.

For both cases, in order to solve the system of equation, it has been used a pressure-based solver, with a fully coupled algorithm, which solves the momentum and continuity equations simultaneously.

As for the discretization scheme it has been chosen the second-order. This is chosen in order to reduce the numerical discretization errors. It is known that while the first-order discretization generally yields better convergence than the second-order scheme, it generally will yield less accurate results, especially on tetrahedral grids.

E. Determination of a sufficiently converged solution.

Convergence can be hindered by a number of factors. Large numbers of computational cells, overly conservative under-relaxation factors, and complex flow physics are often the main causes. There are no universal metrics for judging convergence. Residual definitions that are useful for one class of problem are sometimes misleading for other classes of problems. Therefore it is a good idea to judge convergence not only by examining residual levels, but also by monitoring relevant integrated quantities such as lift coefficient.

For most problems the criteria of convergence is that the scaled residuals decrease to 10^{-3} for all equations. Sometimes this criterion may not be appropriate. Typical situations are listed below.

- If a good initial guess of the flow field is made, the initial continuity residual may be very small leading to a large scaled residual for the continuity equation. In such a situation it is useful to examine the un-scaled residual and compare it with an appropriate scale, such as the mass flow rate at the inlet.
- For some equations, such as for turbulence quantities, a poor initial guess may result in high scale factors. In such cases, scaled residuals will start low, increase as non-linear sources build up, and eventually decrease. It is therefore good practice to judge convergence not just from the value of the residual itself, but from its behavior. It has to be ensured that the residual continues to decrease (or remain low) for several iterations (say 50 or more) before concluding that the solution has converged.

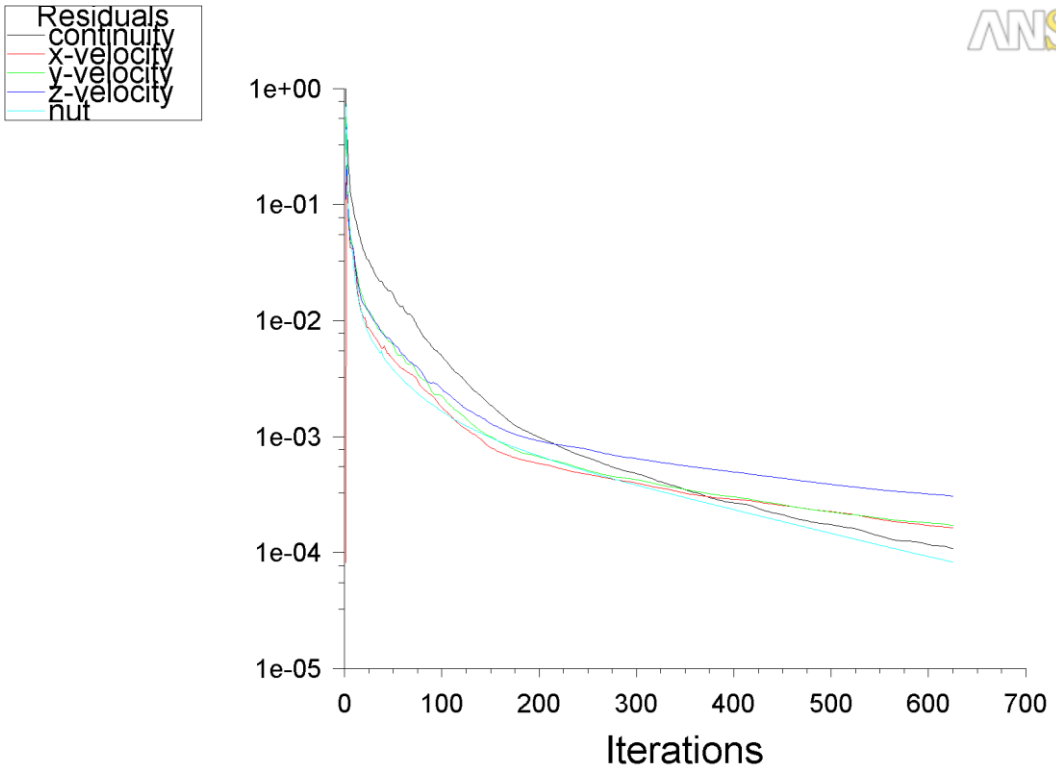

Figure 26 Residuals convergence history

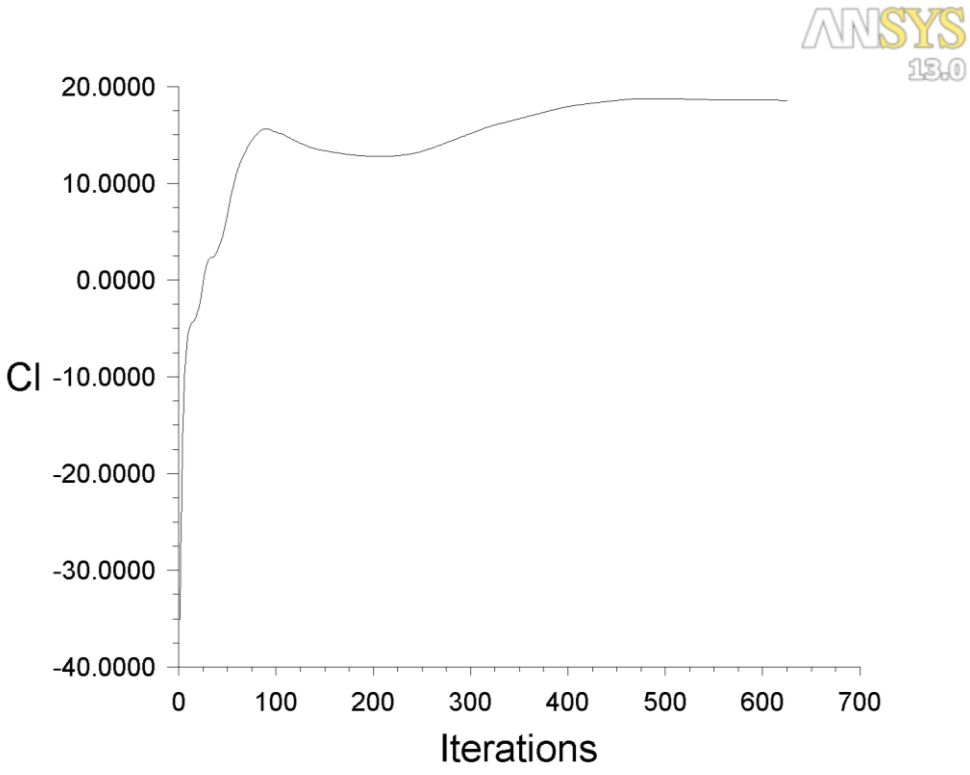

Figure 27 Lift coefficient convergence history

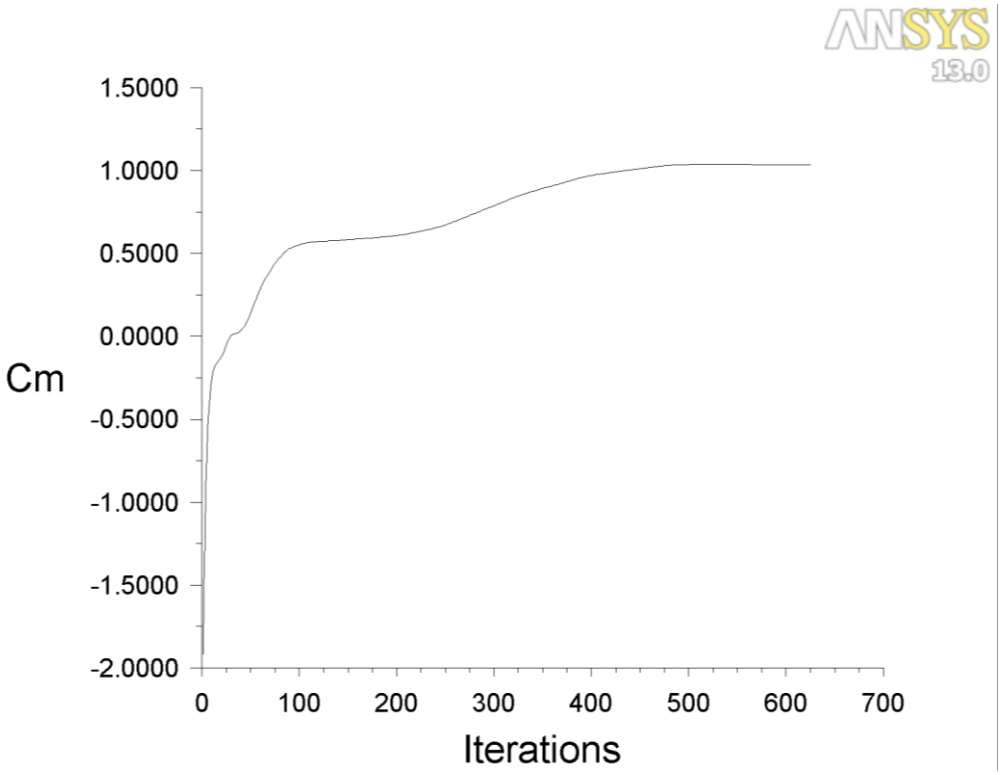

Figure 28 Moment coefficient convergence history

As mentioned above it can be considered that the convergence has been reached when residuals reached a certain level (as it has been set to 10^{-3}), it can be noticed in Figure 26 that residuals reached the required level at about iteration 200. Nevertheless in Figure 27 and Figure 28 it can be noticed that at iteration 200 the lift and moment coefficient are not converged, therefore the simulation was continued until the difference between two consecutive iterations was less than 0.1%. Therefore the final solution was achieved at about iteration 625, after about 100 iterations with the requested error.

F. Post Processing & G. Solution Verification and Validation

The post-processing of the data and validation of the results will be made in a separate chapter.

9. RESULTS

The rate of revolution is kept constant whereas the inflow speed is varied to achieve different advance ratios. Below are tabulated the results of the CFD analysis. In Table 4 and Table 5 are presented the thrust and torque obtained by the simulation, from the first case with the full propeller, comparative with the one obtained from the experiment (see Appendix A4). It can be noticed that the biggest difference is about 16%, which can be considered roughly as acceptable.

Table 4 First case results – Thrust T

No.	v [m/s]	J [-]	$T_{computed}$ [N]	$T_{measured}$ [N]	Δ [%]
1	1.5	0.4006	562.894	653.97	-16.4
2	2	0.5341	539.030	583.92	-8.5
3	2.5	0.6676	458.797	517.02	-12.9
4	3	0.7985	407.960	450.84	-10.1
5	3.5	0.9314	347.091	385.7	-10.7
6	4	1.0683	276.085	318.74	-15.7

Table 5 First case results – Torque Q

No.	v [m/s]	J [-]	$Q_{computed}$ [N.m]	$Q_{measured}$ [N.m]	Δ [%]
1	1.5	0.4006	41.480	35.385	14.5
2	2	0.5341	36.055	32.073	10.8
3	2.5	0.6676	32.923	29.013	11.6
4	3	0.7985	29.773	26.071	12.7
5	3.5	0.9314	25.584	23.102	10
6	4	1.0683	22.278	19.907	10.4

In the table below is presented the comparison of the efficiencies, where it can be seen that it has been underestimated by over 30%, which it is unacceptable for this case of analysis.

Table 6 First case results – Efficiency η_0

No.	v [m/s]	J [-]	$\eta_{0\ computed}$ [-]	$\eta_{0\ measured}$ [-]	Δ [%]
1	1.5	0.4006	0.216	0.294	-36.1
2	2	0.5341	0.317	0.386	-21.7
3	2.5	0.6676	0.370	0.473	-27.8
4	3	0.7985	0.435	0.549	-26.2
5	3.5	0.9314	0.502	0.618	-23.1
6	4	1.0683	0.526	0.680	-29.2

Below are presented the non-dimensional coefficients of thrust and moment and the efficiency, computed as specified in Chapter 4.

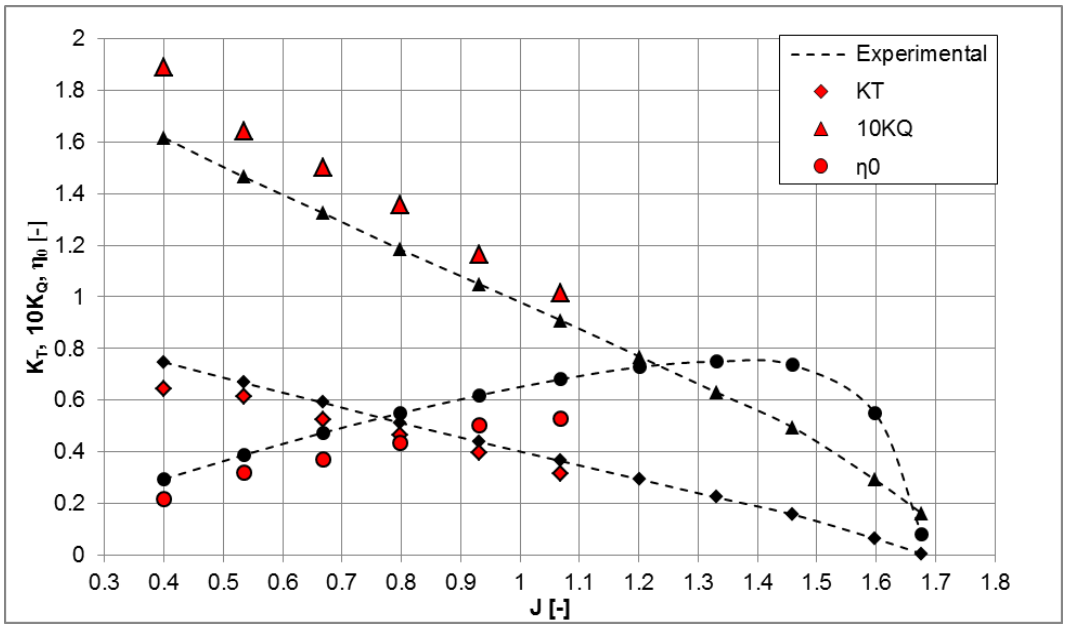

Figure 29 CFD vs. Experimental (first case)

Hence the results were unsatisfactory, due to the big differences between the computed values and the experiment, the need for a second case has arisen. Therefore the second case has been considered, with only one blade and a higher mesh density around the propeller, as presented in Chapter 8. In Figure 30 is depicted the comparison between the experiment and the second case simulation, whereas in Table 7, Table 8 and Table 9 are presented the numerical results.

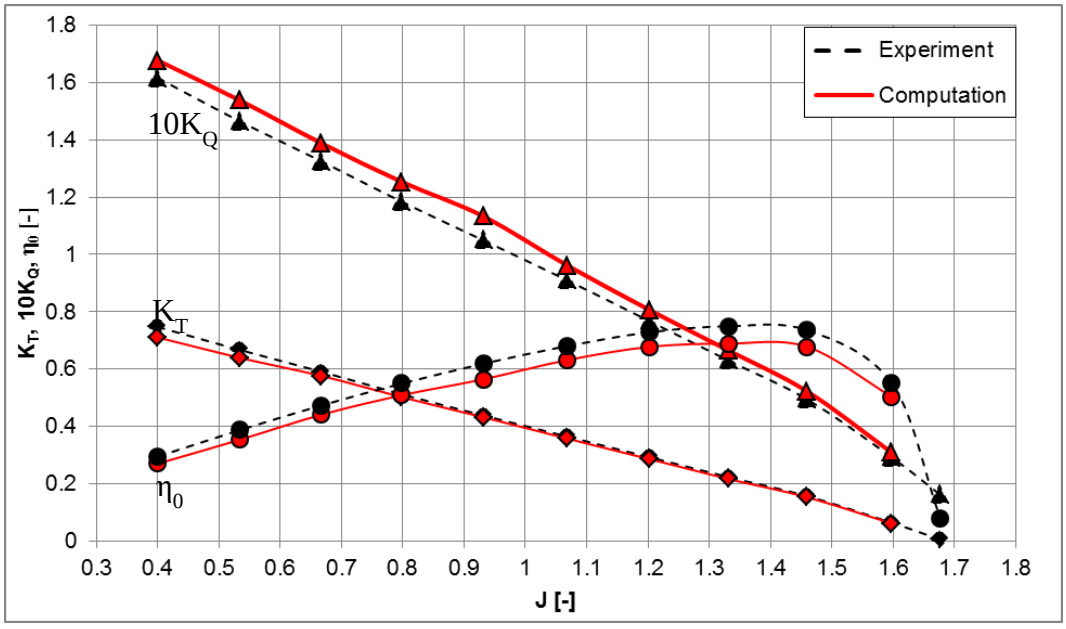

Figure 30 CFD vs. Experimental (second case)

Table 7 Second case results – Thrust T

No.	v [m/s]	J [-]	Tc [N]	Tm [N]	Δ [%]
1	1.5	0.4006	623.4	653.9	-8
2	2	0.5341	561	583.9	-5.1
3	2.5	0.6676	505.4	517	-4.3
4	3	0.7985	440.5	450.8	-2.5
5	3.5	0.9314	378.7	385.7	-1.9
6	4	1.0683	313.4	318.7	-1.5
7	4.5	1.2021	250.7	255.6	-1.9
8	5	1.3308	189.9	196.4	-2.3
9	5.5	1.4594	133.8	138.9	-3
10	6	1.5978	53.5	55.6	-2.7

Table 8 Second case results – Torque Q

No.	v [m/s]	J [-]	Q_c [Nm]	Q_m [Nm]	Δ [%]
1	1.5	0.4006	36.8	35.385	3.65
2	2	0.5341	33.75	32.073	4.76
3	2.5	0.6676	30.46	29.013	4.53
4	3	0.7985	27.5	26.071	5.55
5	3.5	0.9314	24.87	23.102	7.41
6	4	1.0683	21.1	19.907	5.40
7	4.5	1.2021	17.7	16.791	4.83
8	5	1.3308	14.6	13.88	5.31
9	5.5	1.4594	11.46	10.968	5.33
10	6	1.5978	6.759	6.419	5.39

Table 9 Second case results – Efficiency η_0

No.	v [m/s]	J [-]	$\eta_{o\ computed}$ [-]	$\eta_{o\ measured}$ [-]	Δ [%]
1	1.5	0.4006	0.270	0.197	-5.55
2	2	0.5341	0.353	0.294	-9.1
3	2.5	0.6676	0.440	0.386	-9.52
4	3	0.7985	0.508	0.473	-7.39
5	3.5	0.9314	0.564	0.549	-7.95
6	4	1.0683	0.631	0.618	-9.63
7	4.5	1.2021	0.677	0.680	-7.79
8	5	1.3308	0.688	0.728	-7.5
9	5.5	1.4594	0.677	0.749	-8.8
10	6	1.5978	0.503	0.735	-8.52

Further on, due to the poor quality of the prediction of the characteristics of the propeller from the first simulation, only the results from the second case will be considered. For the plots where the whole propeller appears, the domain has been revolved just for visualization purposes.

In Figure 31 and Figure 32 are presented the axial velocity in longitudinal and transversal section, for the case with 1.5 [m/s] speed of advance. It can be noticed that at the tip of the blade the axial velocity is increased considerably. Figure 33 shows the contour plot of pressure distribution in the same section (x=0).

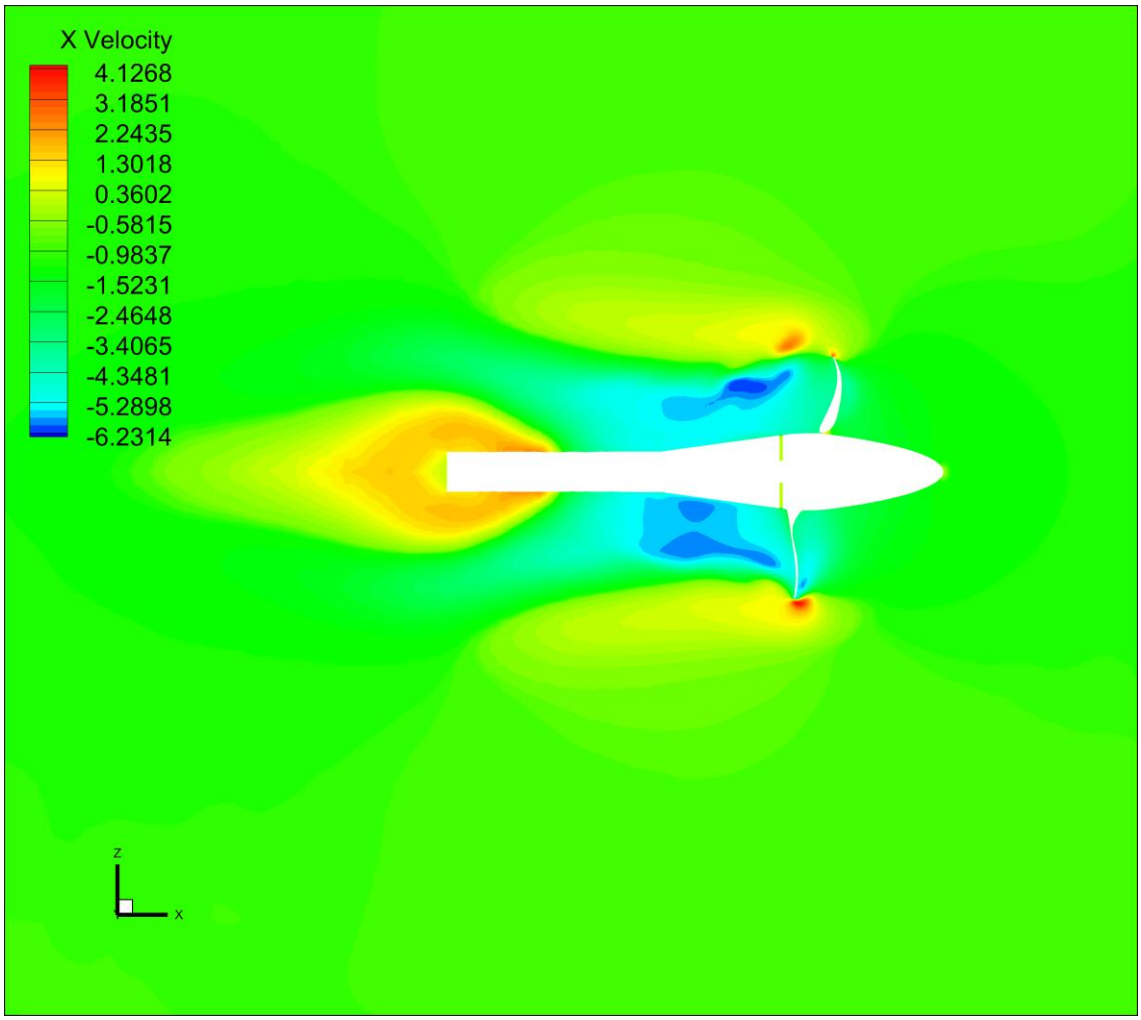

Figure 31 Axial velocity – longitudinal view (y=0, *J*=0.4)

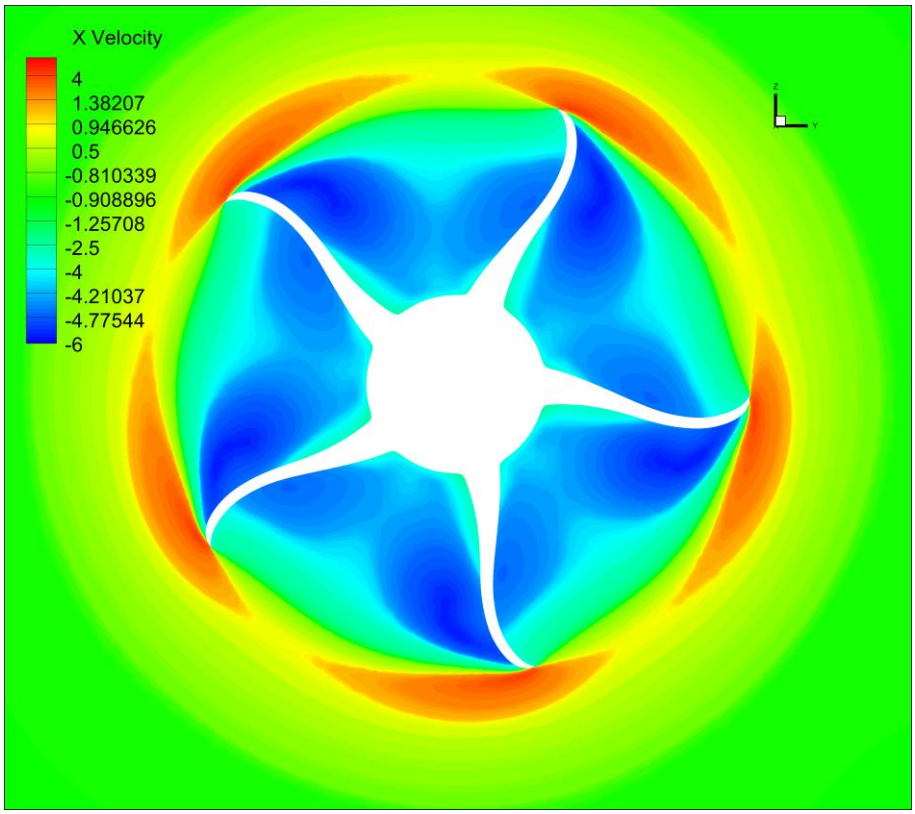

Figure 32 Axial velocity – sectional view (x=0, *J*=0.4)

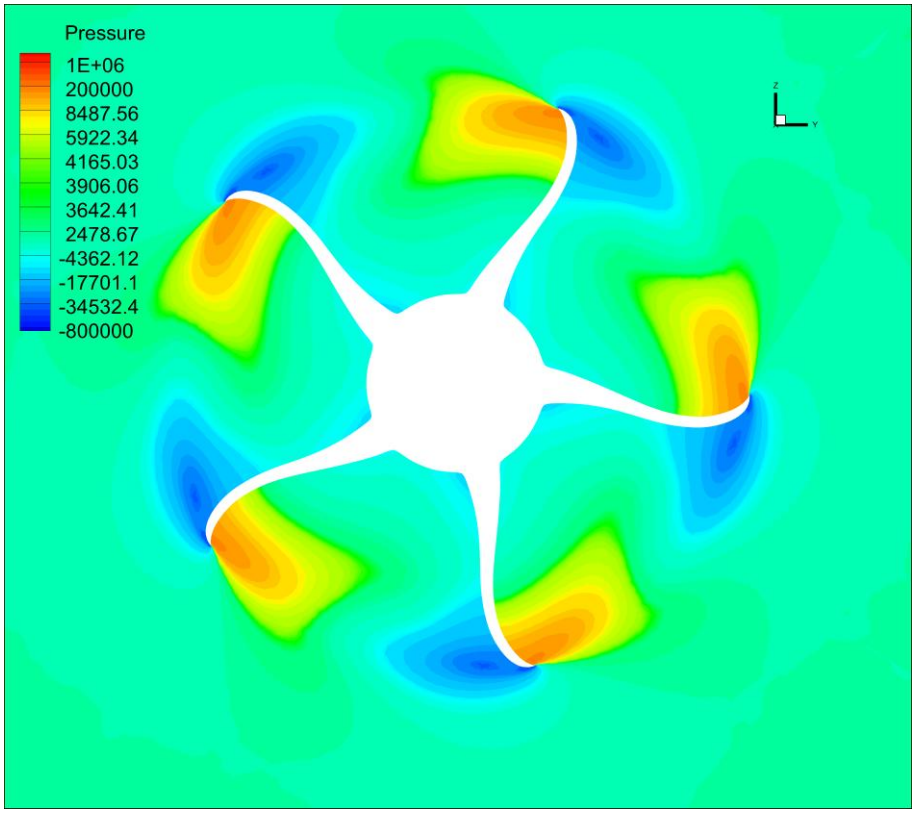

Figure 33 Pressure distribution – sectional view (x=0, *J*=0.4)

In Figure 34, Figure 35 and Figure 36 are presented the contours of the pressure for three radial sections (r/R=0.4, r/R=0.7, respectively r/R=0.9), computed at *J=1*. For each of the contours, the pressure coefficient has been plotted over the length of the chord. It can be noticed that the pressure is higher on the pressure side of the blade than on the suction side, and that it increases with the relative radius. Also it can be observed that the pressure coefficient is higher close to the leading edge. Moreover with the increase of the relative radius, the pressure and the pressure coefficient are more uniform distributed over the chord of the blade.

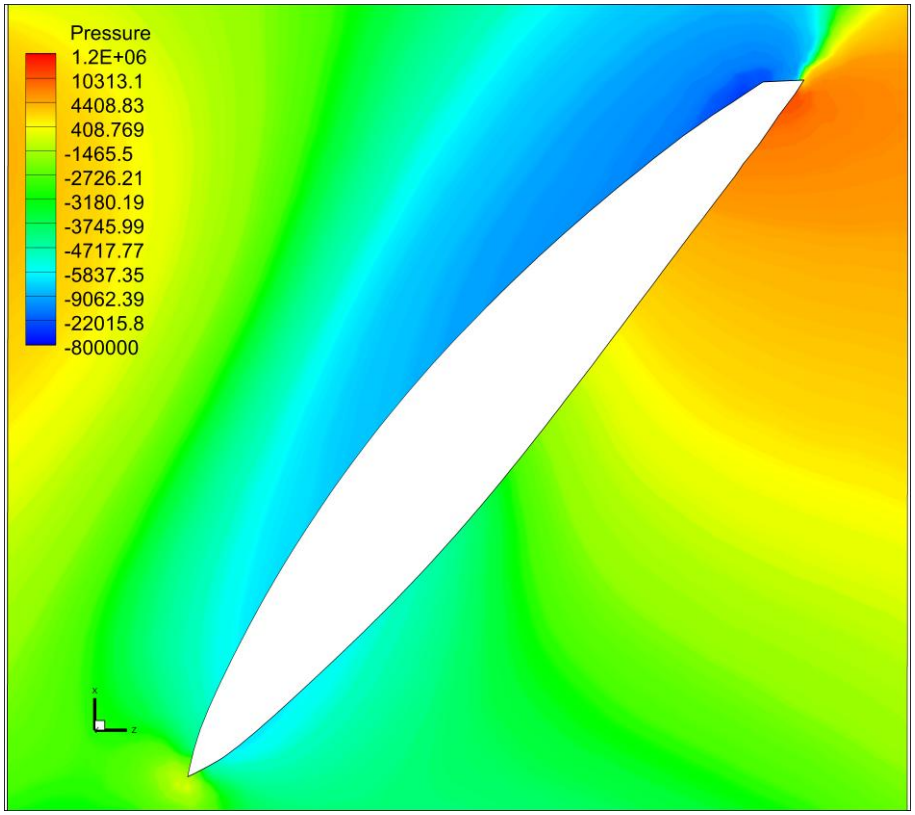

Figure 34 Contour of pressure coefficient at r/R=0.4

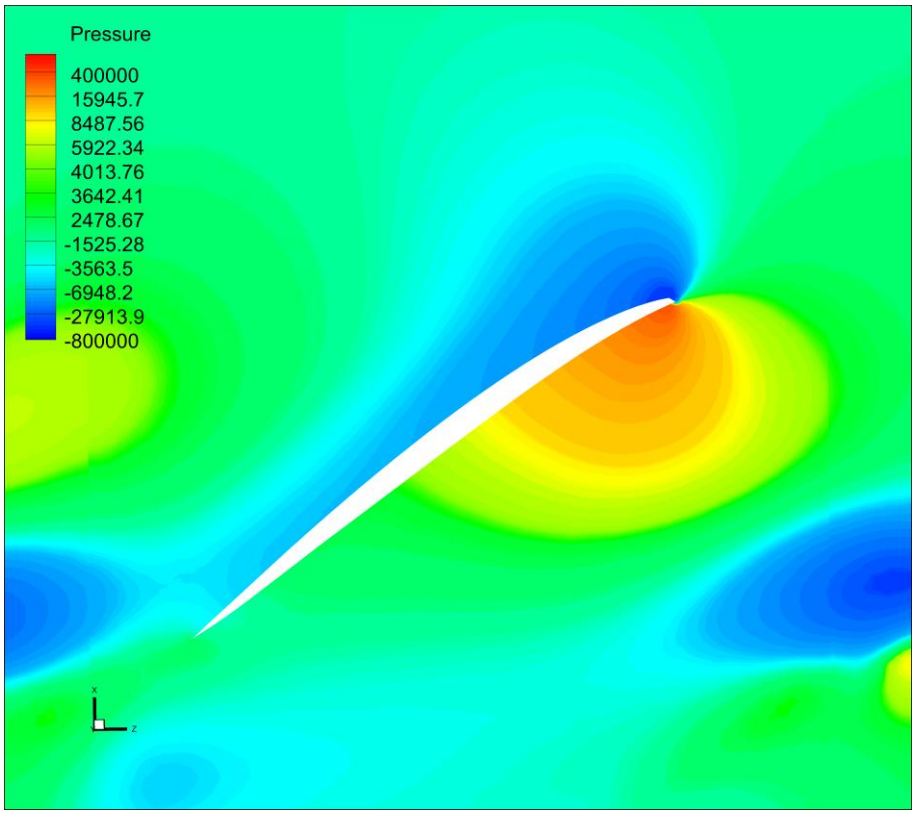

Figure 35 Contour of pressure coefficient at r/R=0.7

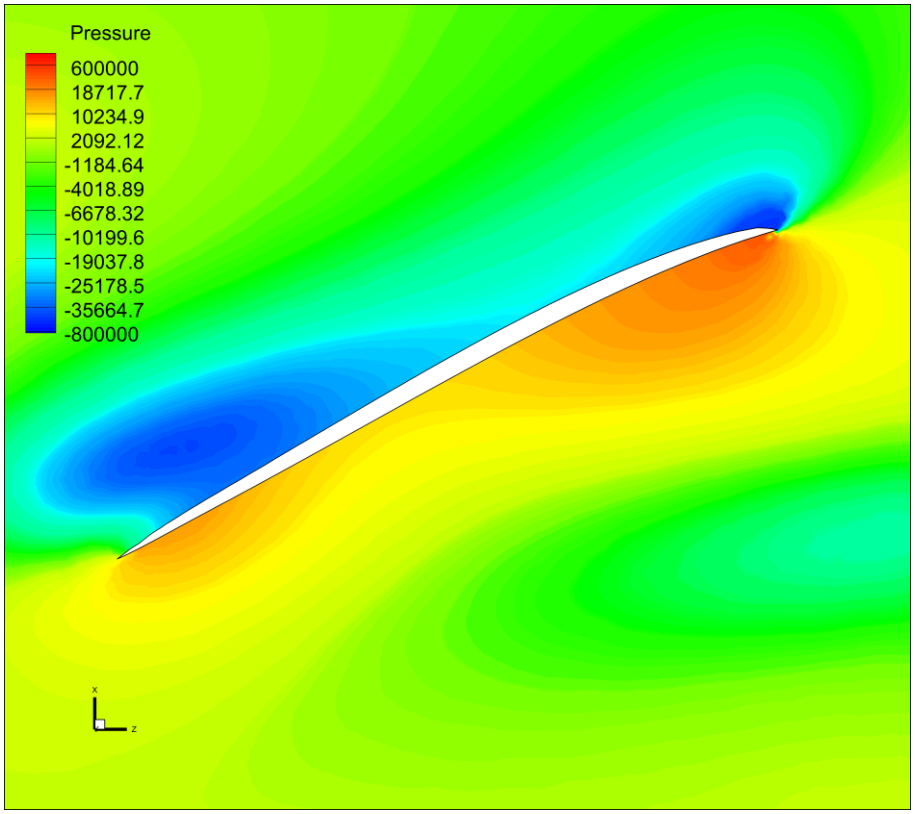

Figure 36 Contour of pressure coefficient at r/R=0.9

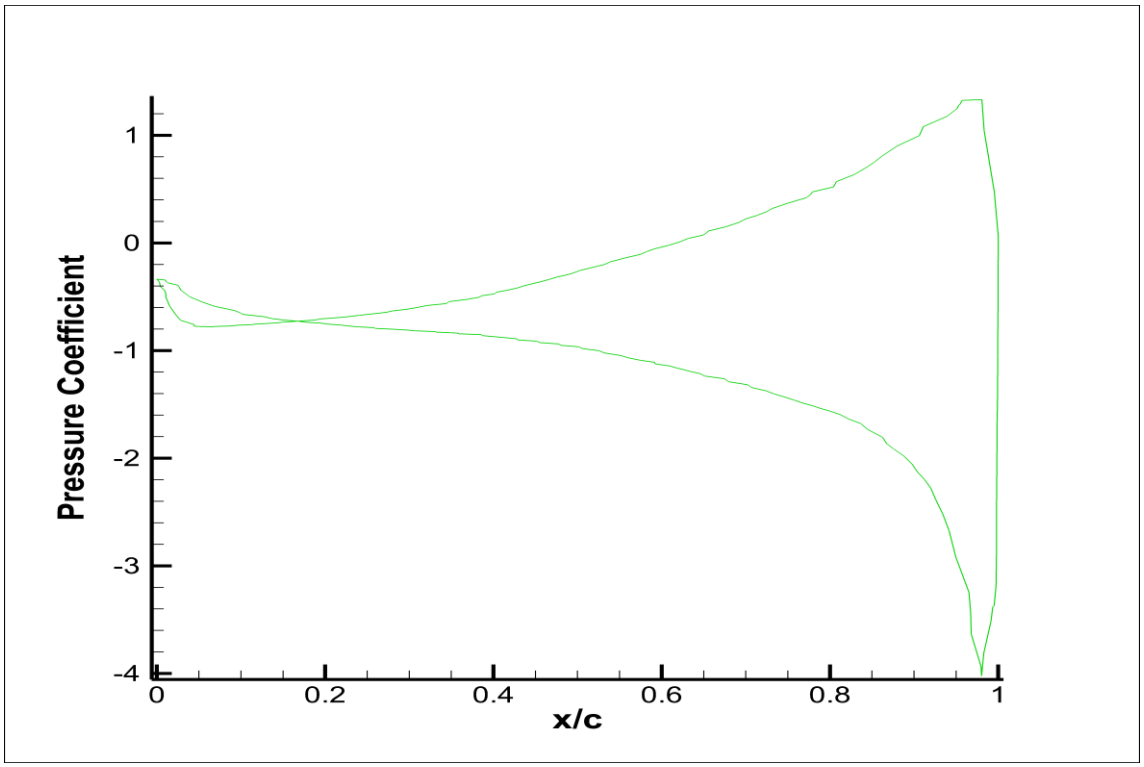

Figure 37 Pressure coefficient distribution over the blade at r/R=0.4

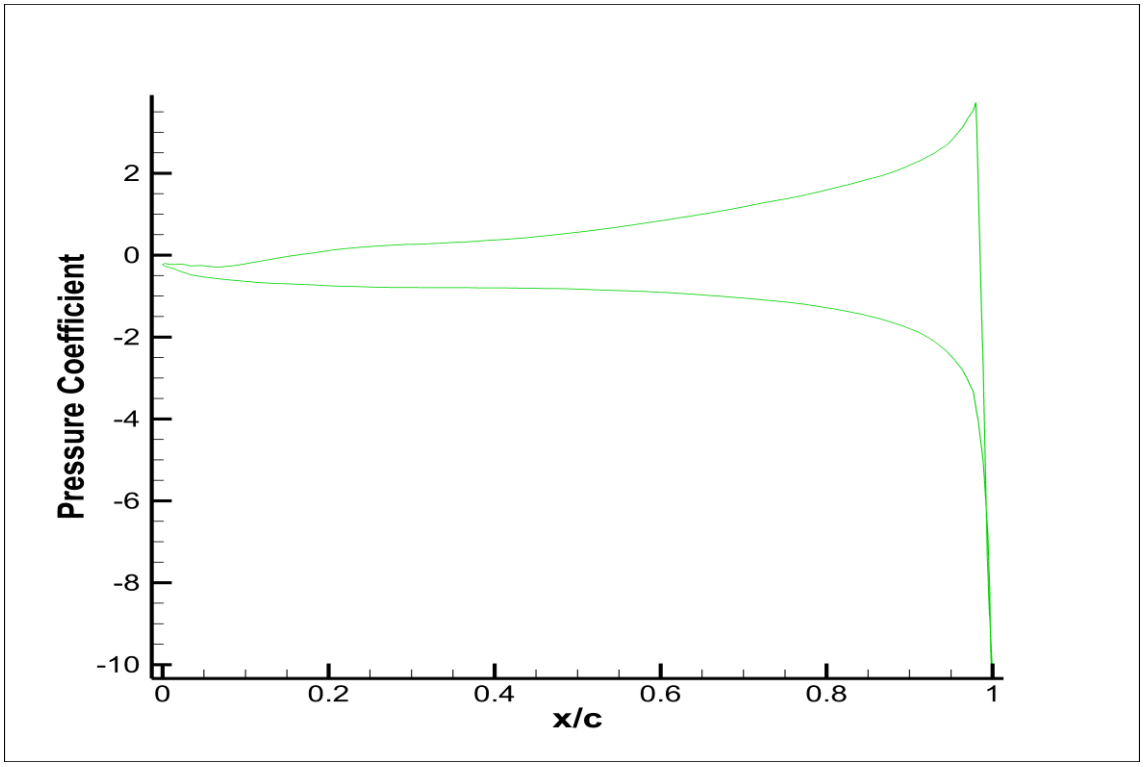

Figure 38 Pressure coefficient distribution over the blade at r/R=0.7

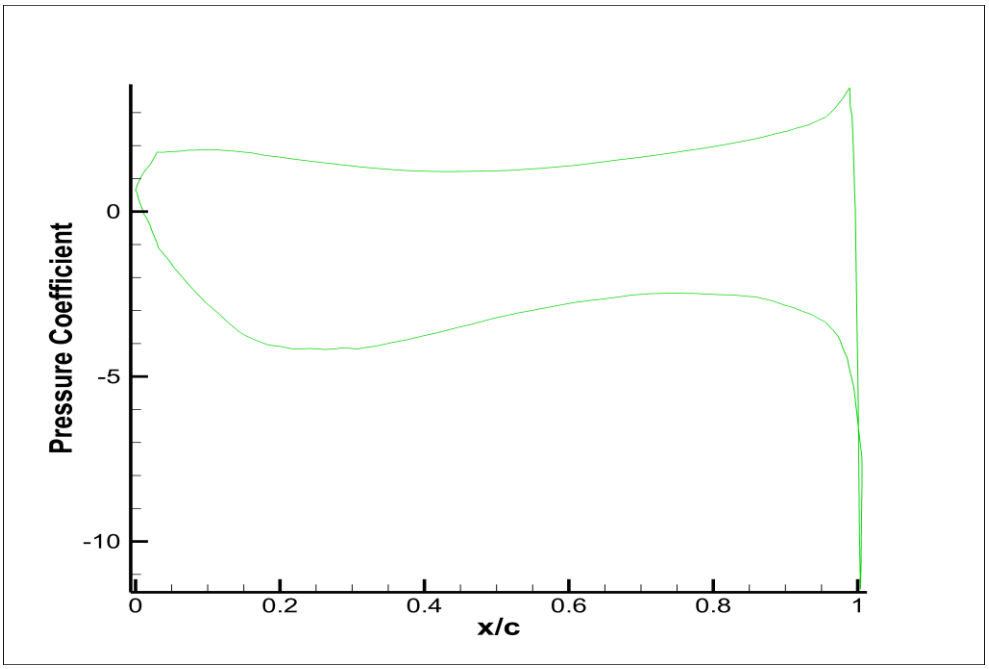

Figure 39 Pressure coefficient distribution over the blade at r/R=0.9

Figure 40 and Figure 41 shows the contour plot of pressure coefficient (Cp) distribution on the pressure and suction side of a blade. The values obtained at an advance ratio *J=1.2* can be compared with the plots obtained by Li [17] at *J=1.243*. It can be observed that the minimum value is located at the tip vortex core slightly downstream the blade tip, while the maximum value is at the leading edge. The Cp is non-dimensionalized using (39), according to the reference.

$$C_P = \frac{(p - p_0)}{0.5\rho(nD)^2} \tag{39}$$

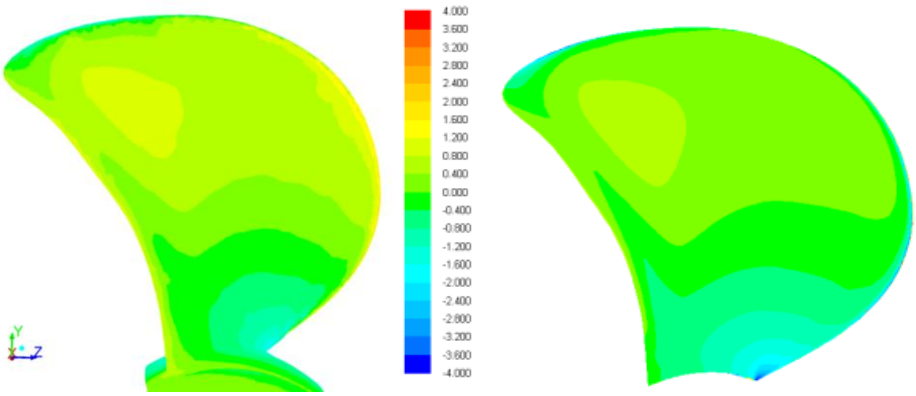

Figure 40 Pressure coefficient comparison on pressure side (*J*=1.2) between own computation (left) and reference [17] (right)

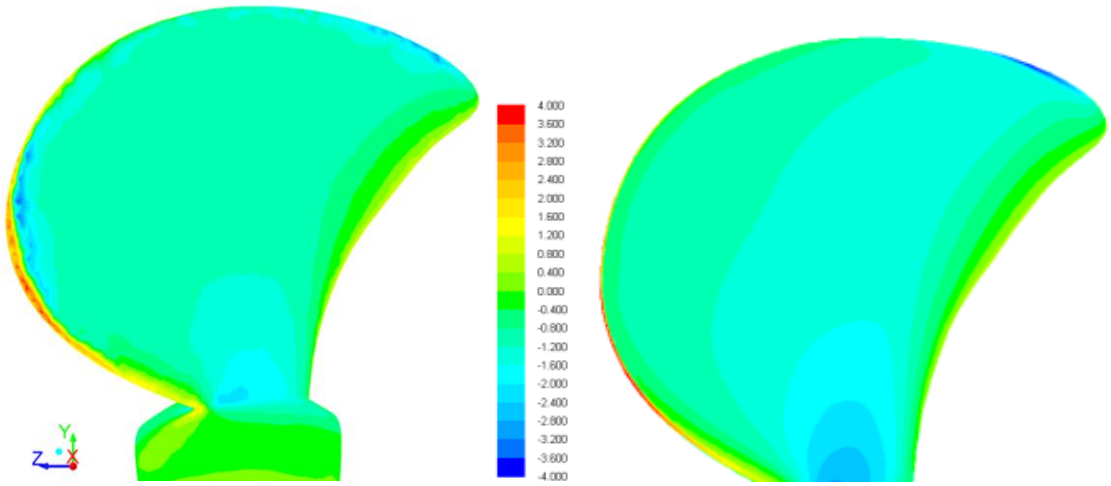

Figure 41 Pressure coefficient comparison on suction side (J=1.2) between own computation (left) and reference [17] (right)

In order to visualize the vortical flow, it is used the vorticity. The vorticity is a derived scalar quantity representing the magnitude of vorticity, and is a measure of the rotation of a fluid element as it moves in the flow field. It is defined as the curl of the velocity vector:

$$|\omega| = |\nabla \times u| \tag{40}$$

In Figure 42 is presented an iso-surface of vorticity of magnitude |ω|=1000. For a better visualization, in Figure 43 is presented an isometric view of an iso-surface of vorticity of |ω|=800. These plots indicate the existence of a tip vortex downstream the blade, as well as its rapid dissipation further downstream.

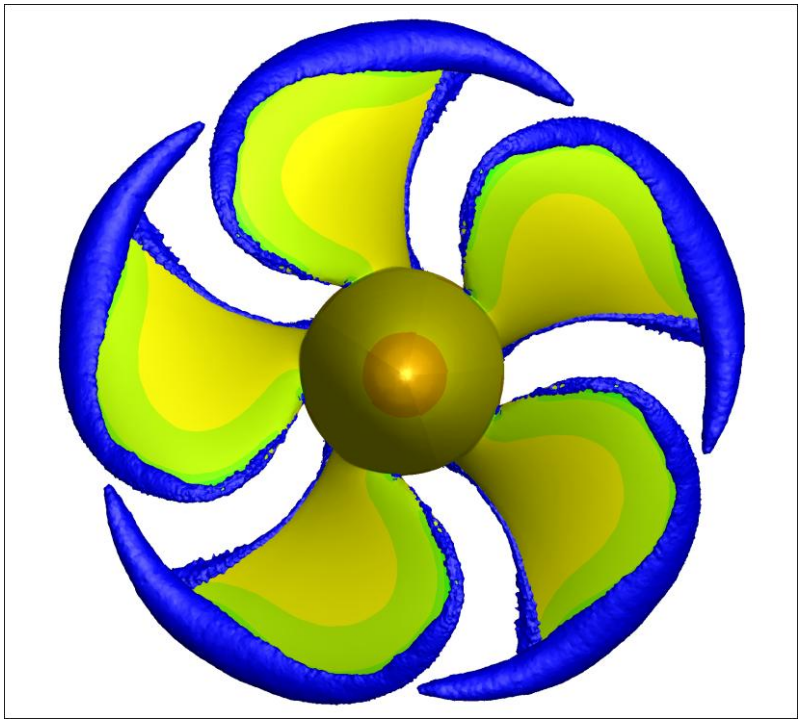

Figure 42 Visualization of the tip vortex

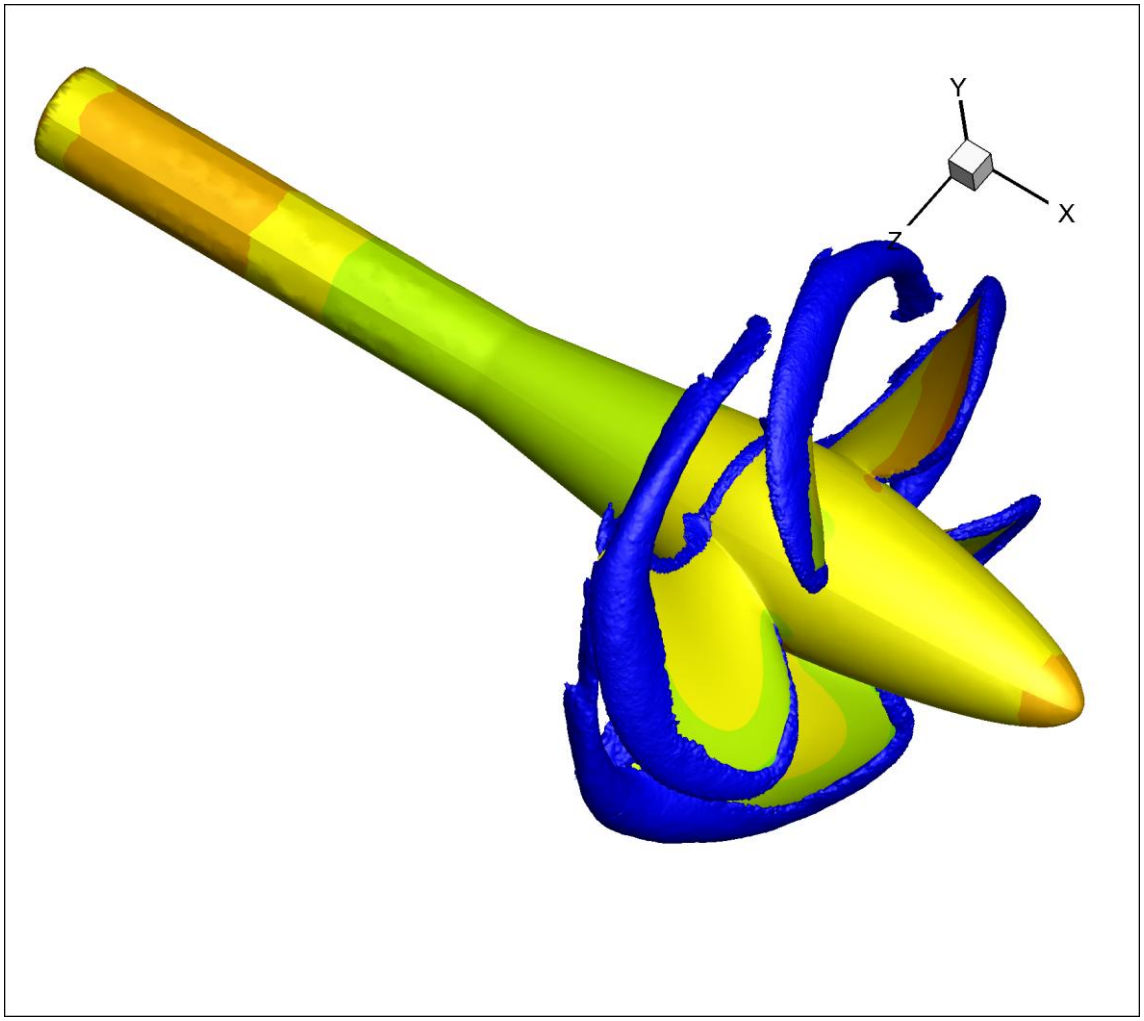

Figure 43 Isometric view of the vorticity

10. CONCLUSIONS

By means of numerical simulations the present work aimed at: understanding the physical mechanisms and to develop an algorithm which will permit to predict the open water characteristics of a propeller.

It has been showed that propeller characteristics are a very important matter, which are driven by economic means, and lead to an increased need for accurate prediction. As it was discussed there are two main methods of predicting the open water characteristics of a propeller: experimental and numerical.

It was being taken advantage of the fact that recently a propeller that has been tested, and provided with extensive experimental results, made available to the public all the data concerning the workshop that has been done on it. Therefore the studied propeller was a five blade, pitch controllable propeller with a high pitch ratio and a pronounced skew.

In order to compute the open water characteristics, first of all, the concept has been defined; so, thrust, torque and efficiency of a propeller have been explained. After which the methods of investigation have been proposed, among which there have been chosen: the lifting line theory and CFD computation using a RANS solver.

Using the open source program, OpenProp v2.4.6, based on lifting line theory, was obtained the open water characteristics, and as it could be seen in Figure 14, the thrust and torque were overestimated. Also the maximum efficiency is obtained at J=1.8 while according to the experiment it is reached at J=1.2. This verifies with the literature in which is mentioned that for modern propellers, with complex geometry, meaning here high skew and pitch ratio, the lifting line theory isn't suitable to analyze the open water characteristics. Nevertheless it can be used in the design process, but only as an initial tool, which must be followed, in the analysis step, by other methods of prediction, more accurate.

Further on, a CFD method has been employed, using the commercial software ANSYS FLUENT. As a first attempt the whole propeller has been taken in consideration and the domain was considered as a cylinder, big enough to avoid any boundary interaction. The computational domain was meshed with about 4 million tetrahedral cells, which eventually turned out to be not so efficient (mesh resolution wasn't good around the propeller, and also it needed quite some computational power). Therefore a new domain has been created representing one fifth of the first one containing one of the five blades of the propeller. This operation was possible due to the fact that the inflow to the propeller is uniform and because

of the rotational movement, which can facilitate the use of periodic boundary conditions. Both cases were considered steady, with incompressible flow.

The open water characteristics in wetted (non-cavitating) conditions were analyzed over a wide range of advance numbers. The analyses were performed with the shaft positioned behind the propeller imitating the test configuration. In order to verify the results, they were compared with the data provided by the towing tank. Additionally they were paralleled with other CFD results submitted to the workshop (see Figure 40 and Figure 41).

It was observed in Table 7 to Table 9 that the results from the second CFD case are more accurate than the other cases analyzed. It can be denoted that the most important thing in a CFD analysis is the mesh generation. Even though it takes a longer time to discretize the domain using user-defined functions on the geometry, the result will be more valuable.

An important remark is related to the tip vortex in Figure 42, the grid behind the propeller has to be small enough to capture the exact vorticity phenomena. Also a good estimation of the angle of the vortex would help a lot in economizing the number of cells, by refining only on the path of the current.

It was observed in Figure 31 that at the end of the shaft there are some turbulent flows which can affect the convergence of the solution. In order to avoid that problem the shaft of the propeller could be modeled until the end of the domain.

Based on the above observations, the author’s knowledge in the CFD field have significantly increased, giving the possibilities for the future analysis to be less time consuming with even more realistic results.

11. REFERENCES

[1] Amorăriței, M., 2008, "COMPLEMENTE DE HIDRODINAMICA ELICELOR NAVALE ÎNCURENT NEUNIFORM", Galați University Press

[2] Amorăriței, M., 2011, "Propulsion–Propeller theory", EMSHIP Lecture, Galați

[3] Anderson, J.D., Jr., Grundmann, R., Degrez, G., Dick, E.,Degroote, J., 2009 "Computational Fluid Dynamics – An Introduction" , Third edition, Springer

[4] Barkmann U. H., 2011, "Open Water Tests with the Model Propeller VP1304", "Potsdam Propeller Test Case(PPTC)", 3752 (1), 1-32

[5] Blazek, J., 2001, "COMPUTATIONAL FLUID DYNAMICS: PRINCIPLES AND APPLICATIONS", Elsevier

[6] Bertram, V., 2000, "Practical Ship Hydrodynamics", Butterworth Heinemann

[7] B.P. Epps, "OpenProp v2.4 Theory Document," MIT Department of Mechanical Engineering Technical Report, December 2010

[8] Carlton, J.S., 2007, "Marine Propellers and Propulsion", Second edition, Elsevier

[9] Caughey, D.A., Hafez, M.M., 2002, "Frontiers of Computational Fluid Dynamics 2002", World Scientific

[10] Ferziger, J.H., Perić, M., 2001, "Computational Methods for Fluid Dynamics", Third edition, Springer

[11] Fletcher, C.A.J., 1990, "Computational Techniques for Fluid Dynamics 1 – Fundamental and General Techniques", Second edition, Springer

[12] Fletcher, C.A.J., 1987, "Computational Techniques for Fluid Dynamics 2 – Specific Techniques for Different Flow Categories", Springer

[13] Gentaz, L., 2011, "CFD for ship Hydrodynamics", EMSHIP Lectures, Nantes

[14] Javaherchi, T., 2010, Review of Spalart-Allmaras Turbulence Model and its Modifications", http://www.ewp.rpi.edu/hartford/~ernesto/S2011/EP/MaterialsforStudents/Gawronski/Javaherchi2010.PDF

[15] Kuzmin D., 2010, "A Guide to Numerical Methods for Transport Equations", Friedrich-Alexander-Universität-Erlangen-Nürnberg

[16] Le Touzé, D., 2011, "Introduction to the simulation of turbulence", EMSHIP Lectures, Nantes

[17] Li, D.Q., "Prediction of Non-Caviting and caviting Performance of a SVA Potsdam Propeller", Second International Symposium on Marine Propulsors smp'11, Hamburg, Germany, June 2011

[18] Lomax, H., Pulliam, T.H, Zingg, D.W., 1990, "Fundamentals of Computational Fluid Dynamics"

[19] Paterson, E.G., Wilson, R.V., Stern, F., 1998, "CFDSHIP-IOWA and Steady Flows RANS Simulations of DTMB Model 5145", 1st Symposium on Marine Applications of CFD, McLean, VA

[20] R.W. Kimball and B.P. Epps, "OpenProp v2.4 propeller/turbine design code," http://openprop.mit.edu, 2010

APPENDIX A1 – Propeller blade data

vp1304

SIDE VIEW
CLEARANCE CURVE

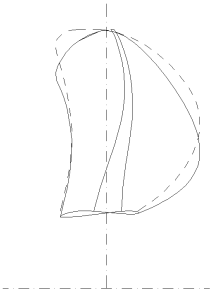

PROJECTED OUTLINE
DEVELOPED OUTLINE

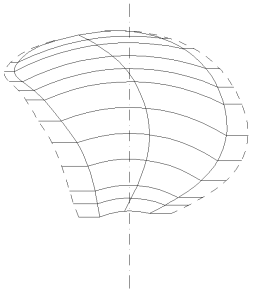

BLADE SECTIONS
EXPANDED OUTLINE

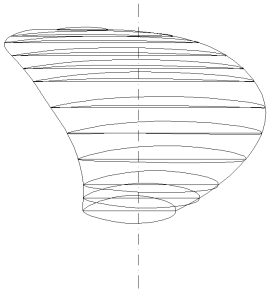

PITCH DISTRIBUTION

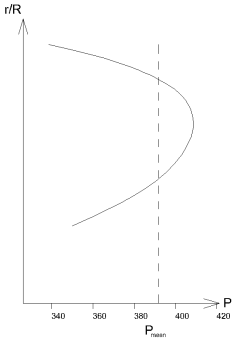

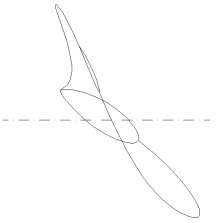

r/R	r	t	c	c_LE	f	rake	P
0.30000	37.50	13.525	45.00	18.25	0.675	0.000	350.00
0.35000	43.75	12.050	56.25	29.63	1.125	-0.500	363.75
0.40000	50.00	10.688	65.42	38.79	1.570	-1.250	376.25
0.50000	62.50	8.137	81.25	52.13	2.356	-3.350	394.50
0.60000	75.00	6.050	94.17	59.83	2.837	-5.875	405.00
0.70000	87.50	4.425	104.17	61.67	3.093	-7.500	408.75
0.80000	100.00	3.250	107.08	56.29	3.052	-7.375	403.50
0.85000	106.25	2.775	106.54	50.93	2.967	-6.625	395.50
0.90000	112.50	2.375	104.17	42.83	2.672	-5.450	382.75
0.95000	118.75	2.013	94.17	29.33	2.194	-4.033	364.50
0.97500	121.88	1.825	78.67	17.00	1.715	-3.300	352.75
1.00000	125.00	1.638	25.00	-14.58	0.500	-2.500	338.75

PROPELLER DIAMETER	D	250.0000mm
PITCH AT r/R=0.7	$P_{0.7}$	408.7500mm
PITCH AT r/R=0.75	$P_{0.75}$	407.3804mm
MEAN PITCH	P_{mean}	391.8812mm
CORDL. AT r/R=0.75	$c_{0.75}$	106.3476mm
THICKN. AT r/R=0.75	$t_{0.75}$	3.7916mm
PITCH RATIO	$P_{0.7}/D$	1.63500
MEAN PITCH RATIO	P_{mean}/D	1.56752
AREA RATIO	A_E/A_0	0.77896
SKEW		19.12428°
HUB DIAMETER RATIO	d_h/D	0.15000
NUMBER OF BLADES	z	5
DIRECTION OF ROTATION		RIGHT-HANDED

APPENDIX A2 – Propeller coordinate system

According to the experimental setup, a propeller coordinate system is defined as follows:

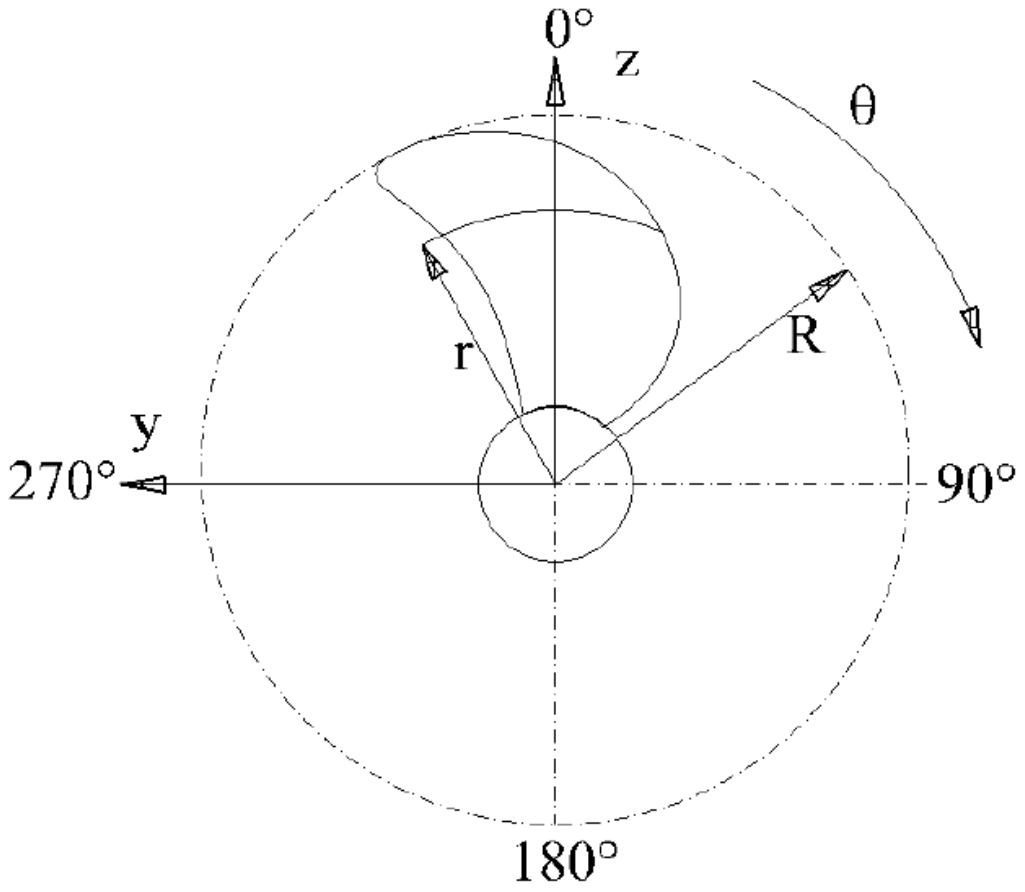

APPENDIX A3 – Basis of Lerbs model

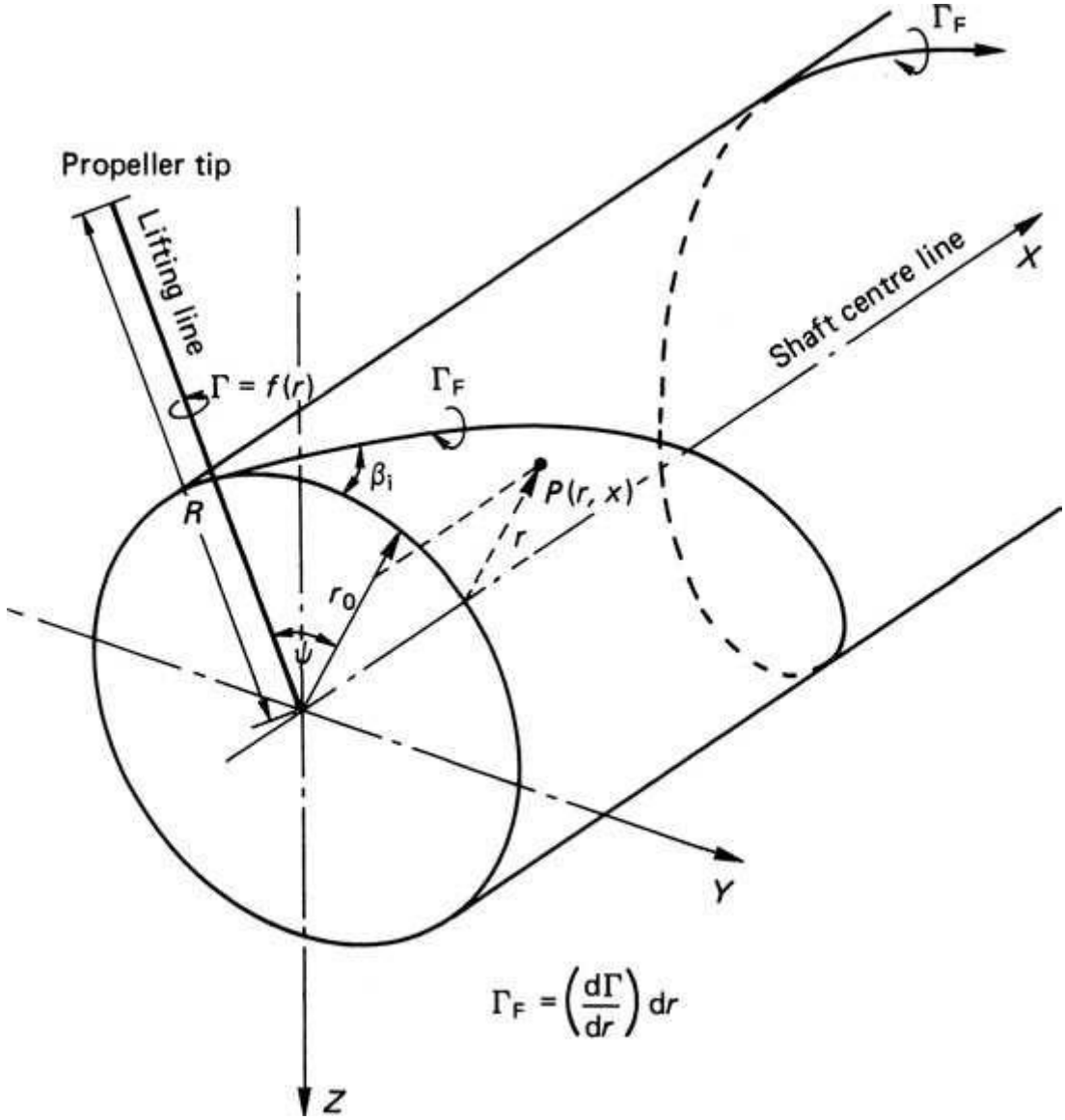

Appendix A4 – Environmental conditions and measured data of the experiment

According to the specifications provided by the workshop [4], the environmental conditions in which the tests have been performed are presented in the following table.

Variable	Value	Unit
Temperature t_w	15.6	^oC
Kinematic viscosity v	1.124e-6	m^2/s
Density ρ	998.99	kg/m^3
Revolution n	15	s^{-1}

The measured values during the experiment are presented below:

No.	v [m/s]	n [rps]	T [N]	Q [Nm]
1	0	14.984	835	45.315
2	0.5	14.984	792.62	42.773
3	1	14.983	727.63	39.186
4	1.501	14.983	653.97	35.385
5	2	14.982	583.92	32.073
6	2.5	14.981	517.02	29.013
7	3	15.026	450.84	26.071
8	3.498	15.023	385.7	23.102
9	4	14.978	318.74	19.907
10	4.5	14.974	255.63	16.791
11	5	15.028	196.45	13.88
12	5.502	15.08	138.95	10.968
13	6.002	15.026	55.6	6.419
14	6.301	15.029	4.17	3.545